Application of quantum light in holography

Abramović, Denis

Sveučilište u Zagrebu

Faculty of Science

Denis Abramović

APPLICATION OF QUANTUM LIGHT IN HOLOGRAPHY

DOCTORAL THESIS

Supervisor(s):
dr. sc. Hrvoje Skenderović
dr.sc. Mario Stipčević

Zagreb, 2022

University of Zagreb

Prirodoslovno-matematički fakultet

Denis Abramović

PRIMJENA KVANTNE SVJETLOSTI U HOLOGRAFIJI

DOKTORSKI RAD

Mentori:
dr. sc. Hrvoje Skenderović
dr. sc. Mario Stipčević

Zagreb, 2022

Supervisors' biographies

Hrvoje Skenderović received his PhD in 2000 working on the spectroscopy of electric discharges at the Institute of Physics, Zagreb. As a Humboldt postdoctoral fellow, he spent two years (2001 – 2003) at the Institute for Quantum Optics in Garching, Germany working on ultrafast dynamics of molecules. After returning to the Institute of Physics he continued to work in the field of femtosecond spectroscopy. He co-authored about 50 papers indexed in WoSCC base and participated at numerous international conferences. His longer stays abroad include TU Wien in 2010. and University of Heidelberg, 2011 – 2012. More recently, his work includes research in digital holography, laser machining and quantum light. He mentored two finished PhD theses and currently mentors two PhD candidates in the field of Optics.

Dr. sc. Mario Stipčević is a senior scientific associate at the Rudjer Boskovic Institute in Zagreb, Croatia (RBI), author of over 100 scientific articles in CC journals cited over 3500 times, 12 invited conference talks, 17 popular articles in the field of electronics and 3 granted patents. He started as nuclear and particle fields scientist in 1991 working on CERN experiments NOMAD and ATLAS. He defended PhD thesis in experimental high energy physics on ATLAS in 1994 at L'Universite de Savoie, Chambery, France. In continuation he worked on CERN's NOMAD, NOMAD-STAR and OPERA experiments as the leader of the RBI's reserach group. Since 2004 his interests turned towards quantum information. In 2011 he was awarded Fulbright scholar at University of California Santa Barbara (UCSB) and Duke University, where he worked on a high speed quantum cryptography. Since 2014 heads Photonics and Quantum Optics Research Unit of Centre of Excellence for Advanced Materials and Sensing Devices at RBI. Research interests: quantum communication, quantum entanglement, quantum randomness, bio-inspired random pulse computer, holography, and neutrino physics. Since 2017 editorial board member of Nature's Scientific Reports. URL: http://www.irb.hr/eng/People/Mario-Stipcevic

Acknowledgments

First, I would like to thank my supervisors Hrvoje Skenderović, Nazif Demoli and Mario Stipčević for all the help and support. It was an interesting experience to see things from, let me say, three different perspectives. I am also indebted to Hrvoje Buljan for several discussions during doctoral studies. My thanks also go to the reviewer of my dissertation, Marin Karuza, Karlo Lelas and Hrvoje Buljan. I also would like to thank Marko Hum from the Faculty of Science for the professional help with all the administrative issues.

I would like to thank for the support obtained from my daughter Ela (now 4 years), mother Ivka and father Ivan, when most necessary. In those challenging days I was very surprised, how you Ela, alone came one evening and brought me a book "Quantenphysik für Babys" (later Ela continued to choose other advanced physics books from which I needed to explain every picture) and asked me serious questions like what does electron do in the atom? I would like to thank my wife Ivana, and the younger daughter Vita (now almost 2 years) for bearing with me, and the beautiful moments that we all had together as a family.

I thank all colleagues and friends that I met during my stay in Vienna, particularly in the group of the leader Anton Zeilinger, where I acquired most of my practical knowledge in the field of quantum optics before embarking on the adventure of PhD in Zagreb. Even during my PhD study, it was nice experience to visit the group of the leader Anton Zeilinger and the group of the leader Rupert Ursin. Special thanks to Sören, Fabian, Joshi, Krishna and Borivoje for some technical discussions during my PhD studies.

Thanks to Ali who was a good friend and a colleague with whom I was able to continue to work on classical holography and twisted light during the last two years or so. I also thank Goran for borrowing one Excelitas detector when necessary; Mladen Pavičić who was willing to discuss some questions in one or another way as well as helping me to get some for me unavailable papers; and Tomislav for an early proofreading during my doctoral study. Thanks also to Vedran, Nikola and Silvija who were good colleagues and with whom I could share some experiences (ups and downs) related to the PhD studies. It was also interesting experience to interact with the cold atom's guys Neven, Ivor, Danijel as well as people from other groups Antonio, Nora, Juraj, Borna and others.

Finally, but not least, I thank Marko Grba, who was willing to listen and discuss all the things that have solidified my passion and curiosity for quantum physics, foundations of physics and beyond for so many years.

Abstract

Holography is a powerful imaging technique that allows to record both amplitude and phase information over a broad electromagnetic spectrum in a hologram. Classical holography as a part of interferometry is capable of the most precise measurements in industry, applied and fundamental science. However, holography is not yet fully exploited and understood from the most fundamental, quantum perspective. A better understanding of holography can lead to new methods outperforming the classical optics and add substantial knowledge about the world around us.

This dissertation addresses fundamentally and technically challenging task of phase retrieval with single-photon states. Previous efforts in low-light-level holography have been based either on classical light source or complex quantum schemes. Here presented architecture and experimental implementation of quantum holography goes beyond this by demonstrating the basic principle of holography with single-photon states. In this way, a new perspective on a textbook description of the basic holographic principle is given. The measured photon statistics during hologram acquisition show that the nonclassical holograms cannot be explained by the classical wave theory. Remarkably, the reconstructions of non-classical holograms show an improvement in amplitude and phase contrast compared to the classical holograms.

Keywords:

Quantum physics, optics, holography, single photons

Proširenisažetak

Holografija je moćna tehnika snimanja koja omogućuje snimanje amplitudne i fazne informacije u širokom elektromagnetskom spektru u hologram. Klasična holografija kao dio interferometrije sposobna je za najpreciznija mjerenja u industriji, primijenjenoj i fundamentalnoj znanosti. Međutim, holografija još nije u potpunosti iskorištena i shvaćena iz najtemeljnije, kvantne perspektive. Bolje razumijevanje holografije može dovesti do novih metoda koje nadmašuju klasičnu optiku i dati značajni doprinos u razumijevanju svijeta oko nas.

Ova disertacija bavi se fundamentalnom i tehnički zahtjevnom zadaćom vraćanja faze s jedno-fotonskim stanjima. Prethodni napori u holografiji niske razine svjetlosti temeljili su se ili na klasičnom izvoru svjetlosti ili na složenim kvantnim shemama. Ovdje predstavljena eksperimentalna implementacija kvantne holografije ide dalje od toga demonstrirajući osnovni princip holografije sa stanjima jednog fotona. Na taj je način dana nova perspektiva na udžbenički opis zapisivanja holografske informacije. Izmjerena fotonska statistika tijekom akvizicije holograma pokazuje da se ne-klasični holografi ne mogu objasniti klasičnom valnom teorijom. Zanimljivo je da rekonstrukcije ne-klasičnih holograma pokazuju poboljšanje amplitude i faznog kontrasta u usporedbi s klasičnim hologramima. Poboljšanje kontrasta se postiže iskorištavanjem vremenske korelacije između dva emitirana fotona iz izvora i selekcijom detektiranih događaja na temelju te vremenske korelacije i malog vremenskog prozora unutar kojeg se vrši selekcija detektiranih događaja. Tehnika je posebno atraktivna za snimanje amplitudne i fazne slike u uvjetima gdje je kritično snimati objekt s minimalnim brojem fotona.

Ključne riječi:

Kvantna fizika, optika, holografija, foton

Contents

1 Introduction: application of holography for fundamental and practical problems

Holography is a powerful imaging technique that allows recording both amplitude and phase information in a hologram over a broad electromagnetic spectrum. The power of holography relies on interference and thus can be sensitive to the smallest changes in nature. Since the earliest days of holography, the inventor of holography Gabor [1] has aimed to develop holography as a tool that provides one of the most precise images of nature down to the atomic level. Today, classical holography is used in industry, applied (including medicine) and fundamental science for achieving various precise measurements. One of the most beautiful and profound results obtained with electron holography and optical reconstruction is shown in Figure 1.

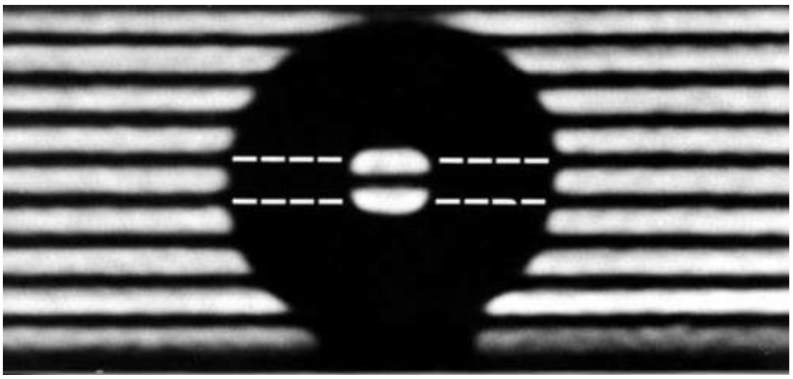

Figure 1. Interference micrograph obtained with an optical reconstruction system. The visible shift of fringes provides evidence for the influence of a vector potential isolated from a magnetic field (one type of Aharonov-Bohm effect [2]). Picture is taken from [3].

Quantum physics provides the most fundamental insight into nature, bypassing the paradigms set by classical physics. Before and after the advent of quantum physics, a large part of physics research was and still is using methods relying on classical physics. Holography is a method that is typically described by classical physics. The goal of the research presented in this doctoral thesis is to gain a better understanding of holography and properties of light in the context of holography from a quantum, single photon perspective. More specifically, an attempt was made to provide answers to the following questions: (i) is it possible to preserves both the amplitude and the phase information in a hologram with single-photon states and pixel-by-pixel scanning, (ii) is it possible to achieve signal-to-noise improvement with single-photon states in comparison to classical holography, and (iii) what are the implications of the experimental results?

2 Theoretical backgrounds: quantum light and holography

2.1 Single photons

2.1.1. Experimental evidence for the existence of single photons

The quantum epoch began with Planck's [4] radical proposal that the elementary quantum of action (energy quantization) exists in the atomic process. Later, Einstein [5] introduced a revolutionary [6] concept according to which the energy of light is a discrete quantity. Planck believed [6] that his proposal could be reconciled with the classical electromagnetic wave theory without using Einstein's idea of the existence of light quanta. The quest for conclusive experimental evidence about the nature of light began. Millikan [7] measured with high precision that the energy of photoelectrons ejected from a material depends linearly on the energy of the incident photon and not on the light intensity as predicted by classical theory. In 1925, Compton [8] showed that the detected energy of a photon is smaller than the energy of a photon incident on an electron and that this is in good agreement with the hypothesis predicted by Einstein that the photon carries momentum [9] and quantised energy [5]. Klemperer's experiment [10] with the coincidence method and the Geiger-Müller counters showed that two photons are detected in positron-electron annihilation [11].

The photoelectric effect and the Compton effect provide strong evidence for the existence of light quanta, but they are not definitive proof of their existence [12]. Until the beginning of the 1970s, the semiclassical models successfully showed that it is not necessary to use Einstein's light quanta to explain the photoelectric effect. In 1974, Clauser performs a conclusive experiment that can only be explained by the hypothesis that light comes in quanta [13]. For the experiment, he uses an atomic cascade process to create photon pairs, which are then sent to the beam splitter. After the beam splitter, the coincidences are measured, that is, simultaneous clicks at two single photon detectors. More precisely, the experimental setup consisted of two beam splitters and a total of four detectors, one beam splitter and two detectors on each side of the experimental setup. The result was the absence of coincidence in the two detectors behind a beam splitter. This was undisputable experimental proof that light was quantized, contrary to the predictions of the semiclassical theories in which light was a classical wave.

The difference between the prediction of the classical wave theory and the particle model of light is illustrated in Figure 2 by the light emission of a single atom. As with the Clauser experiment, the distinguishing criterion between the two models is the measurement of

simultaneous events at different locations (with the same optical distance) in space. In contrast to the particle model, which presupposes that only one event occurs at a time, the spherical wave model predicts that detectors at different locations click simultaneously. According to the classical wave description, the atom emits a spherical wave, which per se can be detected at several locations at the same time. In the case of the particle model, the atom emits a single photon that can only be detected by a single photon detector at one location.

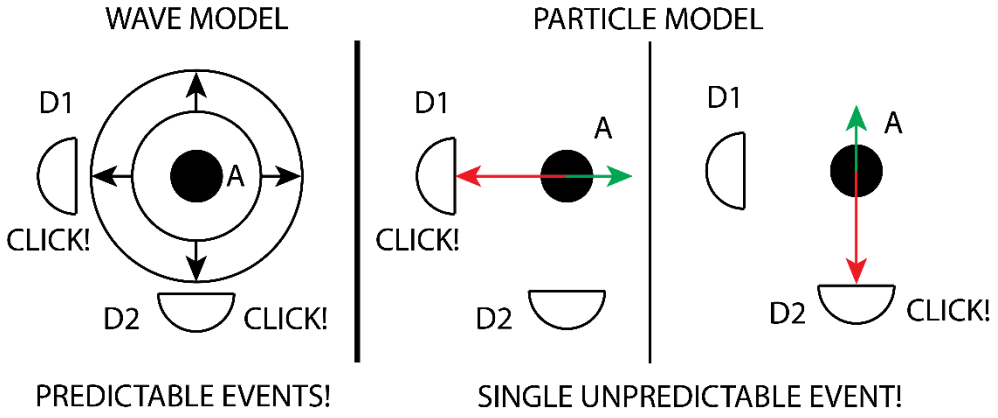

Figure 2. Comparison of two models for an atom that emits light. The thick black line separates the prediction of the wave model from the particle model of light. Black arrows show the direction of wave propagation, red arrows show the place where the emitted photon from the atom has gone, and green arrows show the recoil effect of the atom after the emission of the single photon. The light is detected by single-photon detectors D1 and D2.

Ever since Young's double-slit experiment [14], Taylor's experiment [15] with a feeble light source in the beginning of the 20th century, and numerous interference experiments with different quantum particles [16, 17, 18, 19] have been performed. Interestingly, it often was and still is the case that the experimental apparatus does not consist of a true single-photon (single-particle) generation and detection, either for technical reasons or due to misunderstandings. For a true single-photon (single-particle) experiment (with minimal additional assumptions), in addition to basic physical requirements for the source and detection system, evidence by the measurement of photon/particle statistics is necessary. In Figure 3, the build-up of an interference pattern acquired with single photons and an intensified charge-coupled device [19] is shown. In this experiment, the light source was characterized in a separate measurement setup with two avalanche photodiodes operating in the photon counting regime.

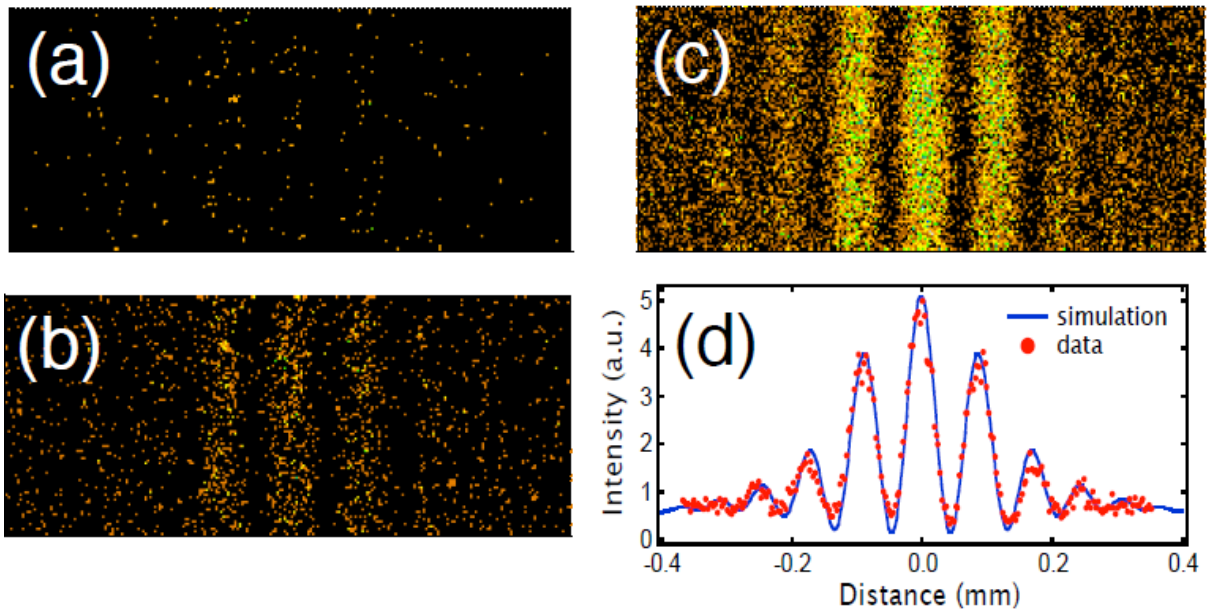

Figure 3. The numbers of single photons are 272 (a), 2240 (b), 19773 (c), binned columns of image and fit (d). Picture is taken from [19].

When the generation and detection of a single photon are properly accounted for, the interference experiment reveals "a phenomenon which is impossible, absolutely impossible, to explain in any classical way" [20]. In a toy model [21], however, the nonclassical nature of the quantum double slit can be overlooked if the generally accepted concept of quantum probability amplitude (standardly related to complex numbers) is neglected. In addition, Feynman [22] makes an important observation about quantum interference in the double-slit experiment: "Although one may be tempted to think in terms of "particle waves" when dealing with one particle, it is not a good idea…" because it is "not like a real wave in space." The quantum wave function lives in configuration space described by complex-valued numbers, and for N particles, the dimension of the configuration space is 3N. Therefore, the quantum wave function can hardly have anything to do with real waves. On the other hand, according to classical deterministic wave theory, it is impossible to explain how (continuous) electromagnetic wave ends up as a localized event. Therefore, the localized events shown in Figure 3 can only be attributed to "mysterious behaviour" [20] of quantum particles, specifically single photons.

2.1.2. Single photons in quantum formalism

The second quantization gives a mathematically elegant way to describe single photons. Energy quantization can be introduced by looking at the quantum harmonic oscillator. The energy jumps can be accounted by introducing annihilation $\hat{a}^{\dagger}$ and creation operator $\hat{a}$, which destroy and create one photon, respectively. This description leads to the introduction of the number operator $\hat{n} = \hat{a}^{\dagger}\hat{a}$. The number operator is then used for the number state representation. The following relations are valid:

$$\hat{n}|n\rangle = n|n\rangle \tag{1}$$

$$\hat{a}|0\rangle = |0\rangle \tag{2}$$

$$\hat{a}^{\dagger}|n\rangle = \sqrt{(n+1)}|n+1\rangle \tag{3}$$

$$\hat{a}|n\rangle = \sqrt{n}|n-1\rangle \tag{4}$$

$$\left[\hat{a}^{\dagger}, \hat{a}\right] = \hat{a}\hat{a}^{\dagger} - \hat{a}^{\dagger}\hat{a} = 1 \tag{5}$$

where $|n\rangle$ is the integer quantum (photon) number and $|0\rangle$ is the ground state (vacuum). Consequently, for a single-photon state, it is possible to write

$$\hat{a}^{\dagger}|0\rangle = |1\rangle \tag{6}$$

2.2. Entangled photons

2.2.1. Experimental evidence for the existence of entangled photons

In 1935, Einstein, Podolsky, and Rosen (EPR) wrote a famous paper [23] in which they considered the relationship between reality and the wave function description of quantum mechanics, including the Heisenberg uncertainty principle. The same year, due to the significance of the raised question, Schrödinger coined the term *Verschränkung* (entanglement) for a system that EPR described. EPR entanglement can be illustrated by a two-particle system in which the two particles interact and then are spatially separated, and a conjugate physical variable is measured. The first question is whether correlations between two interacting particles described by the quantum wave function survive when they are space-like separated. For example, one possibility is that the entangled state is detected as a mixed state. The second, more subtle question is: Is locality, or in other words, signalling at limited speed (of light) between two separated particles a necessary condition for the preservation of entanglement (quantum correlations)? Or in other words, how does the fundamental postulate of the limited speed of light fit into this picture? The third question, which touches on the Heisenberg uncertainty principle, is: if one physical quantity (variable) is measured on one particle and a conjugate physical quantity (variable) is measured on a second particle (which has interacted with the first particle), can it be assumed due to the correlations that all (conjugate) quantities on both particles can be determined with an exact value? The positive answer to the last question would mean that the values are predetermined, even if they are not necessarily predetermined for a single entity (particle) of the system. All this leads to the conclusion that quantum mechanics is either incomplete because the Heisenberg principle is not valid or that quantum mechanics is not complete because the wave function does not describe reality with predetermined properties from the beginning to the spatially separated measuring stations. These questions are not easily answered without empirical data, and even with empirical data, certain new assumptions must be made. In summary, EPR raises challenging questions about quantum theory (in conjunction with the basic postulate of the special theory of relativity, namely, the speed-of-light limit) and its relation to reality.

Bohm reformulated the EPR thought experiment in 1951 [24] for a different physical system and, together with his PhD student, sought an experiment [25] that would provide some other specific answers [26]. Inspired by Bohm's version of the EPR thought experiment, Bell [27] derived an inequality that can distinguish between an alternative theory (local hidden-variable

theories) and quantum theory. Clauser, Horne, Shimony and Holt [28] proposed the first practical test of a Bell inequality in 1969. Two years later, Freedman and Clauser [29] conducted an experiment that showed agreement with quantum theory. They used an atomic cascade as a source of entangled photons, which was later transported to France from the USA. In France, Aspect improved the source and carried out further entanglement experiments [30, 31, 32]. In these experiments, some of the experimental loopholes (assumptions) were removed. Some of the last loopholes were removed with different sources and experimental setups [33, 34, 35]. The results show that alternative interpretations of the EPR thought experiment have been ruled out so far. Finally, to answer some of the questions raised, correlations of entangled states can persist over very large distances even if the entangled particles are separated in space-time, the results of measurements can only be predicted statistically, and EPR correlations are (in this way) compatible with Einstein's light postulate. Of course, it should be noted that faster-than-light signal transmission is not possible, because measurement results can be exchanged most quickly at the speed of light.

2.2.2. Entangled photon pairs in a quantum formalism

Different physical properties can be represented with a quantum state. The most general biphoton state (usually used for the biphoton polarization state) is

$$|\psi\rangle = a|HH\rangle + b|HV\rangle + c|VH\rangle + d|VV\rangle \tag{7}$$

where $|HH\rangle$ is the tensor product $|H\rangle_A \otimes |H\rangle_B$ and so on. The state must satisfy the normalization condition so that $|a|^2 + |b|^2 + |c|^2 + |d|^2 = 1$.

The strange property of a two-particle entangled state is that the state cannot be described as a state consisting of two separate states. In other words, the biphoton state $|\psi\rangle_{AB}$ is an entangled state if it is not possible to factorize to separate states $|\psi\rangle_{A,B}$,

$$|\psi\rangle_{AB} \neq |\psi\rangle_A \otimes |\psi\rangle_B \tag{8}$$

The simplest entangled states consisting of two qubits are Bell's states

$$|\psi^+\rangle = \frac{1}{\sqrt{2}}\left(|HV\rangle + |VH\rangle\right) \tag{9}$$

$$|\psi^-\rangle = \frac{1}{\sqrt{2}}\left(|HV\rangle - |VH\rangle\right) \tag{10}$$

$$|\phi^+\rangle = \frac{1}{\sqrt{2}}\left(|HH\rangle - |VV\rangle\right) \tag{11}$$

$$|\phi^+\rangle = \frac{1}{\sqrt{2}}\left(|HV\rangle + |VH\rangle\right) \tag{12}$$

Bell's states are important states used in EPR experiments. To test EPR correlations, different Bell's inequalities [36] with specific assumptions are used. However, different entanglement measures have been developed that do not rely on the physical assumptions used by EPR. These entanglement measures [37] can be useful for identifying and quantifying specific quantum resources.

2.3. Spontaneous parametric down conversion

In this section, I mostly follow a description of the spontaneous parametric down conversion (SPDC) presented in ref. [38, 39]. Today, the most popular way to generate quantum states of light is via SPDC. In SPDC, an incident photon interacts with an atom through a second-order nonlinear process, thereby inducing a nonlinear (dielectric) polarization response that can generate two photons of lower energy, usually called the signal and idler photons. This process

cannot be explained by classical nonlinear optics [40]. Quantum-mechanically, the interaction Hamiltonian of the pump photon and nonlinear crystal can be written in second quantization as

$$H = \chi^{(2)} a_p a_s^{\dagger} a_i^{\dagger} + H.c. \tag{13}$$

where $\chi^{(2)}$ is the second-order nonlinear susceptibility, subscript *p* is the pump photon, and *s* and *i* are the signal and idler, respectively. Evidently, a high second-order susceptibility is one of the conditions for the process to take place. The operators in the Fock formalism satisfy the conditions stated in section 2.1.2. As seen in the following equation, the two generated photons are in a vacuum state, thus generating two photon pairs in the SPDC process:

$$|1\rangle_p |0\rangle_s |0\rangle_i \rightarrow \hat{a}_p \hat{a}_s^{\dagger} \hat{a}_i^{\dagger} |1\rangle_p |0\rangle_s |0\rangle_i = |0\rangle_p |1\rangle_s |1\rangle_i \tag{14}$$

The simultaneity of photon pair generation was shown by Burnham [41] in 1969. For the generation of down conversion photon pairs, so-called phase-matching conditions, energy and momentum conservation must be fulfilled. Energy conservation requires that the frequencies represented by ω (with a described subscript described before) satisfy

$$\omega_p = \omega_s + \omega_i \tag{15}$$

The wavenumbers represented by $\vec{k}$ (with a described subscript described before) must satisfy inside the crystal,

$$\vec{k}_p \approx \vec{k}_s + \vec{k}_i \tag{16}$$

The $\approx$ sign is due to the uncertainty in crystal length [42]. These conditions can be met in non-centrosymmetric crystals because of nonvanishing $\chi^{(2)}$. More specifically, the process depends on the interaction between the nonlinear coefficient and the pump beam polarization. Therefore, it is possible to distinguish between different types of SPDC: type-0, pump, signal, and idler have the same polarization; type-I, signal and idler have the same polarization but orthogonal to the pump; and type-II, signal and idler have orthogonal polarization.

Phase matching conditions can be achieved for certain nonlinear crystals by birefringent phase matching or quasi-phase matching. Birefringence-phase matching can be introduced by angle tuning or temperature tuning. Quasi-phase matching relies on the structural periodicity of the nonlinear crystal, which is in practice achieved by periodical inversion of the material's nonlinear coefficient. The momentum conservation law for quasi-phase matching is given by

$$\vec{k}_p(\omega_p, n_p(\lambda_p, T)) \approx \vec{k}_s(\omega_s, n_s(\lambda_s, T)) + \vec{k}_i(\omega_i, n_i(\lambda_i, T)) + 2\pi / \Lambda(T) \tag{17}$$

where the wave vector $\vec{k}$ depends on the frequency ω and the refractive index n and the structural periodicity Λ depends on the temperature T. In this way, by tuning the temperature, it is possible to generate photon pairs of different wavelengths. Another advantage is that spatial walk-off (noncritical phase matching) can be eliminated when the pump, signal and idler are collinear. This allows the usage of longer nonlinear crystals as well as easier and more efficient coupling into single-mode fibres.

The spectral profile of down conversion can be approximated by assuming a single frequency pump as follows:

$$I \propto \mathrm{sinc}^2\left(\frac{\mathrm{L}_x \Delta \mathrm{k}_x}{2}\right) \tag{18}$$

where L_x is the length of the crystal, and $\Delta \mathrm{k}_x$ is the wavevector mismatch. The wavevector mismatch is defined as:

$$\Delta \mathrm{k}_x = \mathrm{k}_{p,x} - \mathrm{k}_{s,x} - \mathrm{k}_{i,x} - \frac{2\pi}{\Lambda} \tag{19}$$

The full-width-half-maximum (FWHM) of the spectrum for type-II scales with 1/L. Therefore, a longer crystal gives a narrower FWHM, i.e., a longer coherence length. For example, 10 mm type-II quasi-phase matched nonlinear crystal gives FWHM of 0.55 nm [43].

2.4. Photosensitive detectors

For description of photosensitive detectors presented in this section I refer to the references [44, 45]. Light-sensitive detectors are devices used to record light signals. However, not every light-sensitive detector is sensitive to a single photon. Photodiodes and avalanche photodiodes, for example, are not able to detect a single photon. However, there exist special type of avalanche photodiode that are sensitive to single photons and they are called single-photon avalanche photodiodes. Devices capable of detecting single photons can be divided into two classes: photon-number-resolving detectors and non-photon-number-resolving detectors. The latter cannot distinguish between a single photon and several photons hitting the detector at same time. In practice this means that for a pulse of light with Poissonian distribution, the non-photon-number detector cannot detect the true number of photons. Or, to put in another way, the non-photon-number detector is insensitive to variations in the photon number distribution. A perfect photon-number-resolving detector should clearly detect the number of photons generated by the light source. However, detection efficiency, noise of detector and noise of electronics can distort the true distribution. Detection efficiency reduces the "pillars" of the distribution, and the noises broadens the "pillars". Widening of the pillars can lead to loss of the ability to resolve the number of photons. Some other basic properties of detectors are dark counts, detection efficiency, time jitter, dead time and after pulses. They are defined as follows: dark count is the noise of the detector measured in the absence of external light, detection efficiency is the probability of detecting the photon that reaches the detector, time jitter is the temporal uncertainty in photon detection, dead time is the time within which the detector is basically unable to detect a photon, and after pulses are dark events that occur after a true detection event.

Photodiodes and avalanche photodiodes are based on a reverse-biased p-n junction. The absorption of a photon creates an electron-hole pair. The charge carriers are accelerated by the electric field and interact with atoms through the impact ionisation. As a result of this interaction, a new electron-hole pair can be generated. The process repeats and the charge carriers are multiplied. More precisely, the p-n junction works as a function of the strength of the reverse bias. Photodiodes operate with a low bias voltage and no gain is obtained. However, with a suitable architecture, an approximately linear dependence of the gain on the bias voltage can be achieved. In this mode, an avalanche of charge carriers is generated, which then ceases to the quiescent state. This is a basic principle of the operation of an avalanche photodiode. When the reverse (bias) voltage rises above the breakdown voltage (Geiger region), the

avalanche or multiplication of charge carriers becomes self-sustaining and can only be stopped by external intervention (quenching). In this so-called Geiger regime, photon counting is achieved by the single-photon avalanche photodiodes. Further details on the properties of the single-photon avalanche photodiodes used in this work can be found in the sections 3.4.3 and 4.2.

2.5. Holography

2.5.1. Basic principle of holography

In contrast to photography, which makes it possible to display amplitude information, holography makes it possible to visualize amplitude and phase information. For the invention of holography, Gabor [1] received the Nobel Prize in 1971, when holography has already been applied to a variety of tasks in science, industry, and art. In his Nobel Lecture, he emphasizes that "holography is based on the wave nature of light". Even today, the development of holography is dominantly relying on classical physics. The general principle of holography consists of two steps: the first is the recording of an image that contains the amplitude and phase information, and the second step is the reconstruction of the amplitude and phase information. The information is coded by interference between the reference beam and the beam diffracted from the object. Reconstruction in digital holography is performed numerically from the interference image recorded by a photosensitive sensor or in conventional holography by illumination of a holographic plate. The following analysis is based on image-plane off-axis configuration with assuming aberration-free imaging and the object magnification set to one. The information coding and decoding process can be mathematically described by the following basic equations of holography [46]:

$$\begin{aligned} |\psi|^2 &= |r+o|^2 \\ &= |r|^2 + |o|^2 + ro^* + r^* o \\ &= |r|^2 + |o|^2 + 2|r||o|\cos(\varphi_o - \varphi_r) \end{aligned} \tag{20}$$

$$r \cdot |\psi|^2 = r \cdot |r+o|^2 = r|r|^2 + r|o|^2 + r^2 o^* + |r|^2 o \tag{21}$$

where $|\psi|^2$ is the intensity at the detectors plane, $r = |\mathrm{r}| \exp(-i\varphi_r)$ represents the complex wave function associated with the reference beam, $o = |\mathrm{o}| \exp(-i\varphi_o)$ is the complex wave function coming from the object and the symbol * represents complex conjugate of the given complex wave function. For holography, only the last term of the Equation (20) and (21) is interesting, because this term obviously contains the phase information. All other other terms should be removed to get the object's amplitude and phase information. A numerical procedure for amplitude and phase reconstruction suitable to the image plane off-axis configuration is described below. At the first step (I) a Fourier transform of the recorded image plane hologram is taken so that Equation (20) that describes the fringe pattern takes the following form:

$$FT\left\{|r|^2\right\} + FT\left\{|o|^2\right\} + FT\left\{ro^*\right\} + FT\left\{r^* o\right\} \tag{22}$$

The Fourier transform for two-dimensional (2D) data yields three separated terms, zeroth (first two terms of Equation (22)), minus first (third term), and plus first order (fourth term), in the frequency plane. At the second step (II) an area around plus first diffraction order is isolated and all other points in frequency plane are set to zero. At the third step (III) the inverse Fourier transform is taken on the image obtained in the second step. At this third step, an amplitude and phase image can be constructed. Mathematically, the image obtained in the third step can be written as a two-dimensional complex function:

$$A(\mathrm{x},\mathrm{y}) \exp\left[i\varphi(x,y)\right] \tag{23}$$

where $A(\mathrm{x},\mathrm{y})$ represents amplitude reconstruction and $\varphi(x,y)$ represents phase reconstruction. This phase included a linear phase, $\varphi_r(x,y)$, introduced by the tilt between the reference and object beam, and an object phase, $\varphi_o(x,y)$. Therefore, for a acquiring the objects phase image, the residual reference beam should be removed from

$$\varphi(x,y) = \varphi_r(x,y) + \varphi_o(x,y) \tag{24}$$

If the image described by Equation (23) is multiplied with the complex conjugate of the same image, an image of the object is obtained (IV):

$$A(\mathrm{x},\mathrm{y})\exp\left[i\varphi(x,y)\right]\mathrm{A}^{*}(\mathrm{x},\mathrm{y})\exp\left[-i\varphi(x,y)\right] \tag{25}$$

Next the procedure for the removal of the linear phase term introduced by fundamental fringes due to off-axis beams is explained. In the frequency domain (obtained after first step), a very small area in the centre of the two-dimensional first order is isolated, and again an inverse Fourier transform of the isolated part is made (as in the second step before). This image can be described by a new two-dimensional complex function:

$$B(\mathrm{x},\mathrm{y})\exp\left[i\varphi_r(x,y)\right] \tag{26}$$

where $B(\mathrm{x},\mathrm{y})$ represents amplitude reconstruction. Now, by taking the complex conjugate of Equation (26) and multiplying this with the original image described by Equation (23):

$$\begin{gathered} A(\mathrm{x},\mathrm{y})\exp\left[i\varphi(x,y)\right]B^{*}(\mathrm{x},\mathrm{y})\exp\left[-i\varphi_r(x,y)\right] = \\ A(\mathrm{x},\mathrm{y})B^{*}(\mathrm{x},\mathrm{y})\exp\left[i\varphi_o(x,y)\right] \end{gathered} \tag{27}$$

the object's phase can be extracted. The linear phase could be removed differently, for example, by recording the fringe pattern without the object to obtain $\varphi_r(x,y)$ directly. Remark that by generating a numerical hologram, only a single recording is sufficient to obtain the phase information relevant to the light scattered from the object.

2.5.2. Holography configurations

For the sake of completeness, in this section I briefly discuss various hologram-forming geometries following the references [46, 47, 48, 49, 49, 50]. Essentially, holograms can be recorded using various experimental configurations. In these configurations, it is possible to distinguish geometries according to (i) the collinearity of reference and object beams, which can be on-axis (inline) or off-axis, (ii) the usage of reflective and transmissive specimen, and (iii) the distance between object and hologram. Any combination of these geometries is possible to realize.

Regarding the collinearity of reference and object beams, it is characteristic for Gabor configuration that the reference beam and the object beam are not separated, and the beams are on the same line. However, it is also possible to distinguish another inline configuration from the Gabor configuration, because the reference and object beam can be separated, and the beams can be still parallel. In the case of separated beams, it is easier to control the power of the beams, but in the case of non-separated beams, the setup is less susceptible to technical noises such as vibrations or turbulences from fluids (gas or liquid). Therefore, the basic Gabor setup is particularly suitable for illumination with short coherence length and low photon pair rate.

Inline configurations require a complex reconstruction procedure due to the overlap of the diffraction orders in the reconstruction. One way to avoid this overlap is to use an off-axis setup where the reference and object beams are used at some suitable relative angle. However, the pixel size of the detection system sets limits on how large the relative angle i.e., density of fringes can be. The sampling period should be at least twice the frequency of the (fundamental) interference fringes (Nyquist criterion). For good visibility of the (fundamental) interference fringes, the sampling period should be dense enough to make the sinusoidal pattern of the fringes visible.

Two types of interferometers are commonly used in holography, Michelson and Mach-Zehnder interferometer, both of which can be used with reflective and transmissive specimen. In its simplest form, Mach-Zehnder interferometer is more complex because it uses more optical elements (at least one additional optical element for beam splitting). However, Michelson interferometer is a compact device and equipped with linear translation stage offers possibility to match the path length of the two optical arms relatively easily. This is particularly important when using a source with a short coherence length and weak intensity.

When holography is classified according to the distance between object and hologram, it is possible distinguish between Fourier holography, image-plane holography, Fresnel holography and Fraunhofer holography. Fourier holography can be divided into Fourier holography with lens, lensless Fourier holography and quasi-Fourier holography. These geometries have in common that the reference source must be in the same plane as the object. In Fourier holography with a lens, the object is in the focal plane and the lens performs the Fourier transformation. Characteristic of quasi-Fourier holography is that plane of detection is in the back focal plane of a lens, and the object and the reference point source are coplanar but not in the front focal plane of a lens. Lensless Fourier holography does not use a lens to create a hologram that is in the near-field or Fresnel diffraction region, but still exhibits features of Fourier transform holograms. Besides these geometries, the image-plane holography images the object plane onto the detection plane. The advantage of this configuration is that the image is visible even without Fourier or Fresnel transforms. The imaging optics can also introduce magnification of the object. Therefore, the image-plane configuration is suitable for holographic microscopy. In Fresnel holography, the distance between the object and hologram is usually approximately 10 diameters of the object and the integral of sample radiation requires calculation of one Fourier and one Fresnel transform (integral containing quadratic phase factor), hence the name Fresnel holography. This method is computationally demanding due to the two transforms. Conditions for Fraunhofer holography are satisfied when the holograms are positioned in the far field of diffraction or in other words satisfying Fraunhofer conditions. Fraunhofer holography, for example can be useful for determining the size of small particles.

For holographic measurements, I used a compact modified Michelson (Twyman-Green) interferometer. Michelson interferometer makes possible to choose between different angles between the reference and object beams (on-axis or off-axis). In holography, Michelson interferometer can also be used without a lens (Fresnel setup, lensless Fourier) or with a lens (image-plane setup, Fourier setup or quasi-Fourier setup). Due to the simple numerical reconstruction procedure, the immediate visibility of the object, the flexibility in adjusting the relative incidence angle of beams on the detection plane and the flexibility in moving the mirror position with linear motorised translation stage to match the path length of the optical arms, an advantage was given to image-plane, off-axis, Michelson interferometer with motorised translation stage.

2.6. Quantum description of basic holography principle

Textbook description of the basic equations of holography (Equation 20 and 21) based on classical deterministic physics is given in section 2.5.1. As described there, the basic principle of holography consists of two steps, the first is coding of an image that contains the amplitude and phase information, and the second step is a decoding of the amplitude and phase information. From quantum perspective, the coding process can be described as the quantum superposition of a single particle. The single particle (S) is associated with two probability amplitudes, *r* and *o*, where *r* is the amplitude of the single particle that goes over the reference mirror (M) to the detector (D) and *o* is the amplitude of the single particle that goes over the object (O) to the detector. The information coding process can be described in Dirac notation by following basic equation of holography:

$$\langle D|S\rangle_{\text{via M or O}} = \frac{1}{\sqrt{2}}\left(\underbrace{\langle D|M\rangle\langle M|S\rangle}_{r} + \underbrace{\langle D|O\rangle\langle O|S\rangle}_{o}\right) \tag{28}$$

Equation (28) shows the possible routes that the single particle emitted from the source can take. However, any knowledge of the exact route of the single particle would destroy the single-particle interference that is a necessary ingredient for building an interference pattern particle by particle.

From Equation (28), the probability that the photon reaches the detector (in the detection plane) is

$$P = \frac{1}{2}\left(|r|^2 + |o|^2 + 2|\mathrm{r}||\mathrm{o}|\cos\left(\varphi_r - \varphi_o\right)\right) \tag{29}$$

where $r = |\mathrm{r}|\exp\left(-i\varphi_r\right)$ is probability amplitude associated with reference path and $o = |\mathrm{o}|\exp\left(-i\varphi_o\right)$ is probability amplitude due to the object path. For holography, only the last term of Equation (27) is interesting, because this term contains the phase information. In the proposed image-plane holographic system with an off-axis beams, the phase terms in Equation

(27) can be considered to contain the phase due to respective angle between the reference and object beam. The decoding process can be done by an illumination of the hologram with reference beam or as in this work by the numerical reconstruction (explained in section 2.5.1.).

2.7. Quantum description of Michelson interferometer

In this section, a quantum description of a modified Michelson interferometer (Twyman-Green interferometer) is given. The modified Michelson interferometer uses a reflecting object instead of one simple mirror. By adding an imaging lens (e. g. after the interferometer), this configuration is suitable for recording an image plane hologram. The modified Michelson interferometer (without imaging lens) with inputs and outputs is shown in Figure 4.

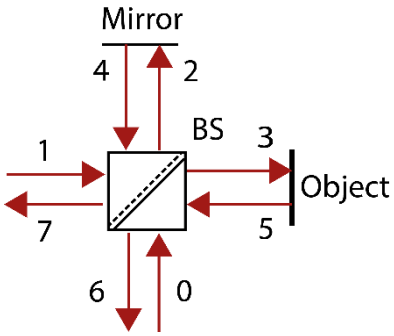

Figure 4. Modified Michelson interferometer. The numbers are associated with the shown (input/output) ports. The two lines (dashed and non-dashed) inside the beam splitter are shown (to conveniently) distinguish between the two possible beam incidence sides of the beam splitter.

The following analysis assumes a lossless (symmetric) 50/50 beam splitter, non-vacuum state at the input port $\hat{a}_1$ and vacuum state at the second input port $\hat{a}_0$. On the other side of the beam splitter are output ports $\hat{a}_2$ and $\hat{a}_3$, respectively corresponding to input ports $\hat{a}_0$ and $\hat{a}_1$ in the transmission direction. When the beams are reflected, the input ports of the beam splitter are represented by $\hat{a}_4 = \hat{a}_2 \exp(i\theta_2)$ and $\hat{a}_5 = \hat{a}_3 \exp(i\theta_3)$. In the direction of transmission, the input ports $\hat{a}_4$ and $\hat{a}_5$ correspond to $\hat{a}_6$ and $\hat{a}_7$ respectively. For the average number of photons at outputs $\hat{a}_6$ and $\hat{a}_7$, the following equations are valid:

$$\langle \hat{n}_6 \rangle = \langle \hat{n}_1 \rangle \frac{1}{2}\left[1+\cos\left(\theta_2-\theta_3\right)\right] \tag{30}$$

$$\langle \hat{n}_7 \rangle = \langle \hat{n}_1 \rangle \frac{1}{2}\left[1-\cos\left(\theta_2-\theta_3\right)\right] \tag{31}$$

The angular brackets $\langle ... \rangle$ correspond to the average value, and $\hat{n} = \hat{a}_i^{\dagger}\hat{a}_i$ is the number operator with the general subscript *i*. The joint probability of detecting a photon in the two output ports $\hat{a}_6$ and $\hat{a}_7$ for the single-photon state is

$$P_{67} = \left\langle \hat{a}_6^{\dagger}\hat{a}_7^{\dagger}\hat{a}_7\hat{a}_6 \right\rangle = \langle \hat{n}_6\hat{n}_7 \rangle = 0 \tag{32}$$

The last relation is without analogy for a classical field [51] and can only be explained in terms of single-photon states. The same output relation as in Equation (32) applies when additional beam splitters are placed before or after the Michelson interferometer. Additional beam splitters and photodetectors behind the two outputs of the beam splitter can be used to check the input state. Based on this fact, I designed an experiment to verify the single photon nature of our illumination and to demonstrate the feasibility of phase retrieval by recording a hologram with single-photon states. Only an input with single-photon state can satisfy Equation (32) and Equation (28) which describes the coding of information.

2.8. Second order correlation function

In this section about second order correlation function, I present the main results showed in reference [12] and the references therein. In quantum formalism, the second order correlation function $g^{(2)}(0)$ behind a 50/50 beam splitter, can be written as follows:

$$g^{(2)}(0) = \left\langle \frac{\left\langle \hat{a}_T^{\dagger}\hat{a}_R^{\dagger}\hat{a}_R\hat{a}_T \right\rangle}{\left\langle \hat{a}_T^{\dagger}\hat{a}_T \right\rangle \left\langle \hat{a}_R^{\dagger}\hat{a}_R \right\rangle} \right\rangle = \left\langle \frac{\langle \hat{n}_T\hat{n}_R \rangle}{\langle \hat{n}_T \rangle \langle \hat{n}_R \rangle} \right\rangle = 0 \tag{33}$$

where the subscript *T* stands for the transmission path and *R* for the reflection path behind the beam splitter. Later in combination with an additional letter in the subscript, the terms refer to double or triple coincidences (three letters in the subscript).

In terms of the operators with a non-vacuum input field $\hat{n}_I^{\dagger}$ and a vacuum field one obtains:

$$g^{(2)}(0) = \frac{\left\langle \hat{n}_I (\hat{n}_I - 1) \right\rangle}{\left\langle \hat{n}_I \right\rangle^2} \tag{34}$$

If the input field is a single-photon state, then obviously $g^{(2)}(0) = 0$, which violates the classical Cauchy-Schwartz relation. The classical Cauchy-Schwartz relation can be written in terms of probabilities *P* for the coincident event (behind the beam splitter) with subscript *TR* and the subscript for single events *T* and *R* as follows:

$$g^{(2)}(0) = \frac{P_{TR}(0)}{P_T \cdot P_R} \geq 1 \tag{35}$$

In case that the detection events are conditioned by a trigger event independent of the optical output ports behind the beam splitter, then it follows:

$$g^{(2)}(0) = \frac{P_{GTR}}{P_{GT} \cdot P_{GR}} \tag{36}$$

where the probabilities *P* are associated with three types of coincidences dependent on the trigger event. More specifically, the subscript letter *G* denotes the trigger events (gate), letters *GTR* denote triple events, and *GT* and *GR* denote coincidences. These probabilities can be written in terms of detection events N as follows:

$$P_{GTR} = \frac{N_{GTR}}{N_G}, P_{GT} = \frac{N_{GT}}{N_G}, P_{GR} = \frac{N_{GR}}{N_G} \tag{37}$$

Therefore, $g^{(2)}(0)$ can be written in terms of detection events as follows:

$$g^{(2)}(0) = \frac{N_{GTR} \cdot N_G}{N_{GT} \cdot N_{GR}} \tag{38}$$

The criterion shown in Equation (38) was used in this work to demonstrate single photon (quantum) nature of light. In addition, to previously described measures for quantifying single-photon source, I introduce normalized second order correlation function for demonstration of photon statistics of marginal (one) arm [52]:

$$g^{(2)}(0) = \frac{N_{TR} \cdot \tau}{N_T \cdot N_R \cdot \Delta t} \tag{39}$$

where N_{TR} is the number of double coincidences, N_T and N_R are the number of single events registered by the two detectors behind the beam splitter, τ is total time of measurement and Δt is the size of coincidence time window. Photon statistics of marginal SPDC arm and of the two SPDC arms can be recorded from same SPDC source simultaneously.

2.9. Model for contrast enhancement

Quantum imaging methods allow imaging that goes beyond conventional classical imaging. Roughly speaking, the advantages of quantum imaging can be divided into two classes: contrast or signal-to-noise enhancement [53, 54] and resolution enhancement [55, 56]. Most quantum imaging techniques rely on either quantum resources such as entanglement or spatial correlation. However, in a simple model that does not assume any complex resource such as entanglement or spatial correlations, England et al. [57] demonstrate (amplitude) image contrast

enhancement using configurable background noise from an independent light source and nonclassical temporal correlations [41] between twin photons. Our experiment and model are also based on a comparison of the method with and without temporal correlations between twin photons but with some important differences. Among the most important features of our experiment is that I demonstrated contrast enhancement for both the amplitude and phase images (by comparing classical and quantum hologram) and that our model does not assume that the probability of registering a noise count is same for method based on temporal and without temporal correlation. In this way, I provide a more realistic model that accounts for the fact that coincidence noise is different from the noise registered in imaging without a temporally correlated technique by a single detector. Another difference is that our method does not require the acquisition of two separate images to quantify the experimental signal-to-noise ratio (SNR). The latter is due to the fact that I separate the hologram image into two regions: the bright region covers an area of constructive interference from which a signal can be registered, while the dark region covers an area of destructive interference or an area from which no signal is expected. In the following subsections, I analyze two techniques: the heralded technique based on temporal correlations between twin photons and the non-heralded technique based on detection of events without temporal correlations.

2.8.1. Heralded signal-to-noise ratio

The following model assumes the generation of temporally correlated twin photons. Ideally, one of the twin photons is detected by the trigger detector (SPCM1 shown in Figure 6, section 3.3.) and the other signal photon by the imaging detector (SPCM4 or SPCM5 shown in Figure 6). If the probability of detecting coincidence signal is denoted as P_{CS}, the probability of detecting coincidence (originating either from signal or noise) as P_C, and the probability of detecting coincidence noise as P_{CN} then $P_{CS} = P_C - P_{CN}$. All the probabilities are stated for detecting an event in a given time bin (coincidence time window). SNR for heralded technique can therefore be defined as

$$SNR_H = \frac{P_{CS}}{P_{CN}} = \frac{P_C - P_{CN}}{P_{CN}} \tag{40}$$

The probability of coincidence noise P_{CN} is composed of probabilities related to the coincidences between the dark count of the imaging detector and trigger detector, P_{DI-T}, coincidences between the imaging detector and the dark counts of the trigger detector, P_{I-DT}, and coincidences between the dark imaging detector and the dark trigger detector, P_{DI-DT}. Using this notation, the probability of coincidence noise is given by

$$P_{CN} = P_{DI-T} + P_{I-DT} - P_{DI-DT} \tag{41}$$

The minus term in the definition of P_{CN} must generally be included, because the dark counts are already included twice in terms that contain P_{DI-T} and P_{I-DT}.

For sake of relating probabilities to experimentally measured counts, it is useful to define the following mean variables: N_{CS} as coincidence signal, N_C as coincidence (originating either from signal or noise) and N_{CN} as coincidence noise. Using this notation, $N_{CS} = N_C - N_{CN}$. All the stated variables can be considered as average counts per pixel during the integration time T at the single pixel. Regarding the number of time bins B, it is necessary to define the coincidence time window Δt within which the coincidences are selected, so that $B = T / \Delta t$. These variables are related to probabilities by following relations $P_{CS} = N_{CS} / B$, $P_C = N_C / B$ and $P_{CN} = N_{CN} / B$. The heralded SNR can therefore be written as

$$SNR_H = \frac{N_{CS} / B}{N_{CN} / B} = \frac{N_C - N_{CN}}{N_{CN}} \tag{42}$$

Note that SNR_H is always ≥ 0, because N_C includes N_{CN} and N_{CS}. The coincidence noise (N_{CN}) is the coincidence noise related to the dark counts of the imaging detector N_{DI}, counts registered by the imaging detector N_I, the dark counts of the trigger detector N_{DT}, and counts registered by the trigger detector N_T. Thus, the coincidence noise can also be written in terms of average counts per pixel during the integration time at the single pixel as

$$N_{CN} = N_{DI} \cdot N_T \cdot \Delta t + N_I \cdot N_{DT} \cdot \Delta t - N_{DI} \cdot N_{DT} \cdot \Delta t \tag{43}$$

The minus term in the definition of N_{CN} must be included, because the dark-dark coincidence noises are included in each of two previous terms on the right-hand side of Equation (43).

2.8.2. Non-heralded SNR

If P_S denotes the probability of detecting a photon (originating either from signal or noise) on the imaging detector (SPCM4 or SPCM5 in Figure 6) and P_{SN} is the probability of detecting a (singles) noise on the imaging detector then the probability of detecting a (singles) signal on the imaging detector $P_{SS} = P_S - P_{SN}$. SNR for non-heralded technique can be defined as follows

$$SNR_{NH} = \frac{P_{SS}}{P_{SN}} = \frac{P_S - P_{SN}}{P_{SN}} \tag{44}$$

By defining following mean variables, N_{SS} as singles signal, N_S as singles and N_{SN} as singles noise, then $N_{SS} = N_S - N_{SN}$. As before, all variables are stated as average counts per pixel during the integration time *T* at the single pixel. Furthermore, all probabilities are related to the maximum number of events *N* that could be recorded without accounting for losses during the

integration time *T*. In this way, $P_{SS} = N_{SS} / N$, $P_S = N_S / N$ and $P_{SN} = N_{SN} / N$. Thus, SNR for non-heralded technique can be written as

$$SNR_{NH} = \frac{N_{SS} / N}{N_{SN} / N} = \frac{N_S - N_{SN}}{N_{SN}} \tag{45}$$

If $N_S \approx N_{SN}$ or $N_{SS} << N_{SN}$ then SNR_{NH} is approximately equal to zero. This is the case when the use of the heralded technique may be particularly beneficial because of the possible noise suppression.

2.8.3. Heralded enhancement factor

Finally, it is possible to express heralded enhancement factor as follows:

$$HEF = \frac{SNR_H}{SNR_{NH}} = \frac{P_{CS} / P_{CN}}{P_{SS} / P_{SN}} = \frac{P_{CS} \cdot P_{SN}}{P_{SS} \cdot P_{CN}} \tag{46}$$

In addition, it is possible to introduce a factor η that takes into account the efficiency that heralded event is included in non-heralded events. In this case $P_{CS} = \eta \cdot P_{SS}$, and heralded enhancement factor yields:

$$HEF = \frac{\eta \cdot P_{SS} / P_{CN}}{P_{SS} / P_{SN}} = \eta \frac{P_{SN}}{P_{CN}} = \eta \frac{N_{SN}}{N_{CN}} \tag{47}$$

It is clear from Equation (47) that the heralded enhancement factor is greater when the noise suppression is greater. The whole analysis can be applied to recorded holograms so that the

signal consists of the photons recorded in areas of constructive interference. Since the detector cannot distinguish between noise and signal, it is possible to define a bright region as an area from which a signal and noise can be registered, while a dark region is defined as an area that is a consequence of destructive interference or an area from which no signal is expected.

In the presented work, I compared the results of the heralded and the non-heralded technique with an approximately equal number of signal photons. The typical coincidence time window for silicon single-photon avalanche detectors has a size of a few ns and is mainly limited by detection jitter. The small coincidence time window leads to a selection of events (coincidences) related to temporal correlations between twin photons. In other words, the imaging detector does not capture all the noise that is detected in the continuous mode of operation, but it captures only events when signal is expected. Therefore, the use of a small coincidence time window is a key factor in noise suppression. However, it should be noted that the noise level in the hologram (interferogram) may be limited by the visibility of the fundamental fringes. For example, the source of this noise can be caused by the ability to distinguish a photon that emerges either from reference or object path. This imposes the maximum possible visibility of interference fringes. Anyway, remark that the previous analysis was made under the assumption that the photon is equally likely to come from either the reference or object arm of the interferometer.

3 Experimental quantum holography

3.1 Background: Low-light-level holography

Besides classical techniques developed for recording holograms in low-level-light conditions with a weak coherent state (attenuated laser) and photon counting [58, 59, 60], quantum concepts using a down conversion light source and complex beam preparation setups for recording holograms were also investigated. These quantum experiments are based on two-photon probability amplitude [61], polarization entanglement [62], one-photon probability with two object beams [63] and interference of two beams from two separate down conversion processes [64]. Strong laser pumping of the down conversion crystal for generating photon pairs can lead to multiphoton pair emission [65, 66], and losses can lead to photon detection without true single-photon characteristics [13] of the experiment. In experiments, often for practical purposes, only an attenuated or not well characterized source is used that cannot fulfil criteria for a single-particle source. Apart from tackling different aspects and technical issues of hologram recording, none of these classical [58, 59, 60] and quantum [61, 63, 62, 64] holographic methods give attention to characterization of the light source with the second order correlation function, $g^{(2)}(0)$. This method is a standard tool [12, 69] used for the characterization and verification of a single-photon source. In complex experiments where the single-photon character is of fundamental interest, the source can be characterized either in a separate setup [67, 68], at certain points during the experiment [69] or during the full course of the experiment [13]. The characterization of the illumination during the full course of the experiment gives maximal experimental assurance that the source maintains the single-photon character, and no additional hypothesis about the character of the light source is necessary.

From the detection perspective, methods in quantum holography either have been based on intensified complementary metal oxide semiconductor (ICMOS) [61, 63] electron-multiplying charge-coupled device (EMCCD) [62, 70] or scientific complementary metal oxide semiconductor (sCMOS) [64]. In classical holography, single-photon avalanche photodiodes also been used for hologram recording [59, 60], but in quantum holography, single-photon avalanche photodiodes have been used only as a trigger signal for the ICMOS [61, 63], which recorded a hologram. Evidently, the possible advantages of using the avalanche photodiode in Geiger mode for recording holograms with a triggering scheme have not been investigated until now. This seems to be a promising avenue of research, as it is known that photon correlations can improve image contrast under certain circumstances [53, 54] and that N-photon number

states with N≥2 can improve resolution [55, 56]. However, no improvement in image contrast has yet been demonstrated for hologram images, which are specific due to interference fringe patterns and the extraction of not only amplitude but also phase information.

3.2 Proposed concept: quantum holography with single-photon states

In this thesis, I present an approach for recording nonclassical digital holograms in a basic holographic scheme with continuously monitored single-photon illumination and single-photon detection. The single photons are generated by the heralded single-photon source in the process of spontaneous parametric down conversion, and the single-photon sensitivity is achieved by the usage of a single photon counting module (SPCM) based on silicon single-photon avalanche photodiodes. The implementation of the single-photon illumination and exclusion of the classical wave theory is supported via a long-run measurement of the second order correlation function, $g^{(2)}(0)$, before and during the two-dimensional multichannel detection in front of and behind the holographic setup. In this way, evidence for the nonclassical character of holograms is established by the measured photon statistics.

Furthermore, the proposed generation and detection scheme based on single-photon states allows the acquisition of holograms with lower noise than classical holography. A comparison of a nonclassical hologram (made from single-photon states) and a classical hologram (made from non-heralded light) is visually shown in holograms, amplitude, and phase reconstructions. For demonstration purposes, I used different amplitude and phase objects.

Three different setups for a hologram recording based on a Michelson (Twyman-Green) interferometer and heralded single-photon source are shown in Figure 5. The first setup (a) assumes that the source is characterized as a single-photon source in a separate experiment, the second setup (b) measures $g^{(2)}(0)$ before the interferometer, and the third setup (c) measures $g^{(2)}(0)$ after the interferometer. In this scheme for the $g^{(2)}(0)$ measurement two detectors behind a beam splitter are necessary.

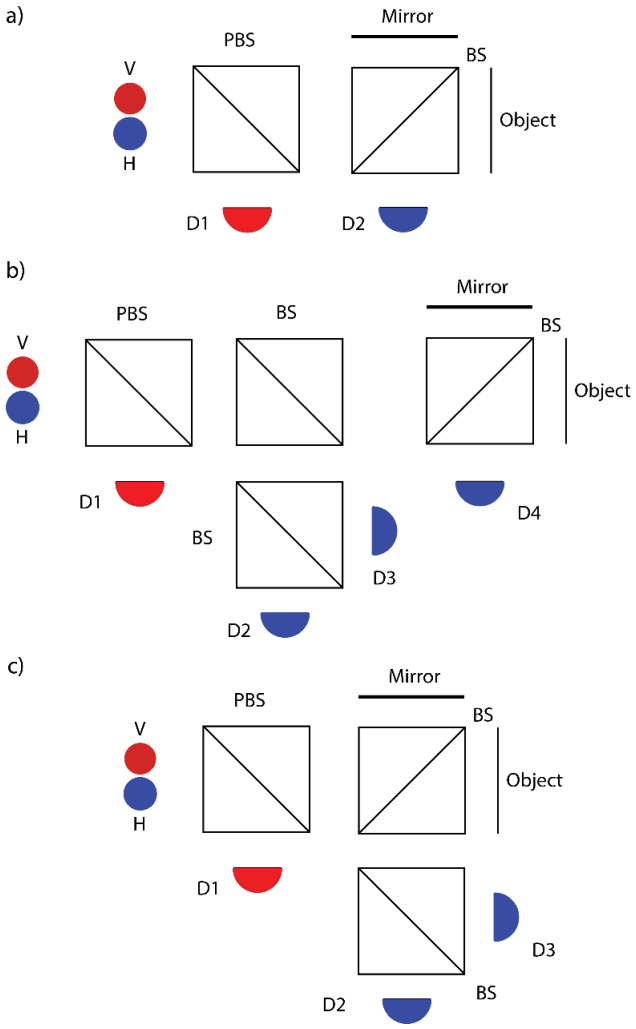

Figure 5. Different holographic setups based on heralded single photons. In all three (a-c) setups, D1 is the heralding (trigger) detector. In the first setup (a), detector D2; in the second setup (b), detector D4; and in the third setup (c), detectors D2 and D3 are the imaging detectors. D2 and D3 are used for continuous characterization of the light source before (b) or after (c) the Michelson interferometer consisting of a mirror, 50/50 beam splitter (BS) and an object.

The temporal correlation between heralding and heralded single photons represents an essential part of single photon generation. Even though necessary, it is not sufficient evidence for an exclusion of classical wave theory. To exclude classical wave theory, I experimentally evaluate the second order correlation function $g^{(2)}(0)$ for the three detectors. I use the experimental definition, introduced in Equation (37), for which $g^{(2)}(0) = N_1 \cdot N_{123} / (N_{12} \cdot N_{13})$, where N_1 is number of single events registered by heralding detector (D1), N_{12} is the number of double coincidences registered between heralding (D1) and heralded detector (D2), N_{13} is the number of double coincidences registered between heralding (D1) and second heralded detector (D3), and N_{123} is number of triple coincidences registered between heralding and two heralded

detectors behind 50/50 beam splitter. The value $g^2(0) \geq 1$ holds for classical wave theory [69] and when $g^2(0) \leq 0.5$ is achieved, then the light source is considered a good single-photon source due to the nonzero projection on the single-photon Fock state, where value closer to zero indicates a purer single-photon state [71]. Furthermore, if the coincidence time window within the heralding and heralded single photons are detected is chosen small enough, the temporal correlation between heralding and heralded single photon can greatly reduce the noise in the image (hologram). This reduction in noise also implies much lower noise fluctuations. However, this does not necessarily imply a strong advantage for the image contrast. Therefore, a practical advantage of this noise reduction is also investigated in this thesis.

3.3. Experimental setup: light source, interferometer, and detection setup

As shown in Figure 6, the experimental setup for single-photon holography consists of three parts: a light source (a), a setup for continuous characterization of the light in front of the interferometer (b), and an interferometric image-plane setup with a scanning single pixel detection and characterization system (c). The characterization setups consist of two single-photon detectors and can be used for continuous measurement of the second order correlation function. In the case of heralded light, the light source acts as a single photon source, and in the case of non-heralded light, the source acts as a source of thermal states. However, from the perspective of our experimental setup, the photon statistics for non-heralded light is very similar to a Poissonian [52]. All the relevant parameters for the photon statistics are averaged out due to resolving times much larger than the coherence time of the down-converted photons. Therefore, it can be considered that thermal states generated in the SPDC are practically imitating coherent states in terms of photon statistics. The coupling of the photon pairs into the single-mode fibers destroys the spatial correlations between the twin photons. By measuring the cross-correlations before the start of the holography experiment, time delays between the different optical arms were determined. This information was used for convenient measurement of coincidences.

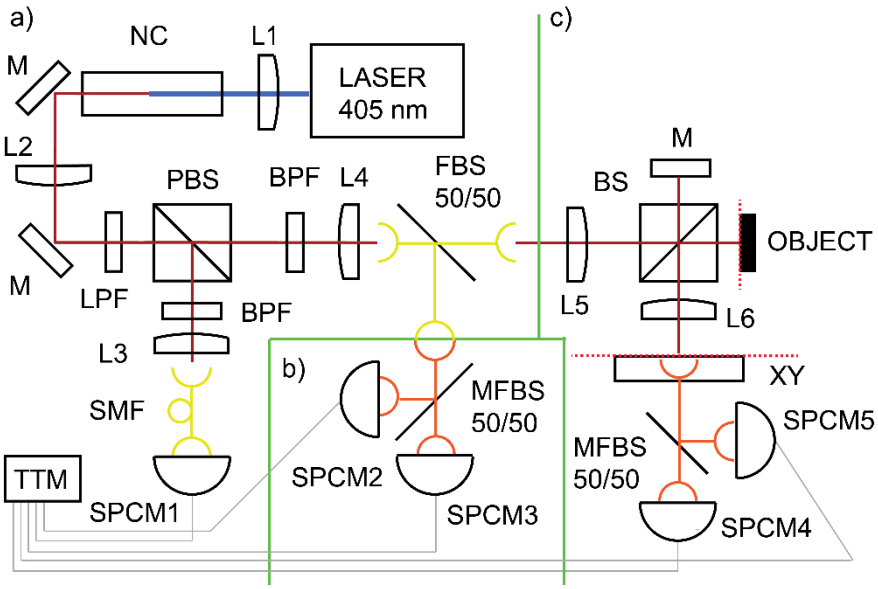

Figure 6. Experimental setup for recording non-classical holograms with single photons. In part (a), a single frequency (volume Bragg grating stabilized) diode laser illuminates nonlinear crystal (NC) to produce collinear, orthogonally polarized, and degenerate photon pairs at 810 nm. The laser beam passes a focusing lens (L1) and is blocked by a longpass filter (LPF). The down-converted photons are collimated by a lens (L2) and further filtered from background light by a bandpass filter (BPF) designed with central wavelength of 810 nm. The vertically polarized photons reflected from a polarizing beam splitter (PBS) are focused and coupled into a single mode fibre through an aspheric lens (L3) and detected by the detector SPCM1. The second, horizontally polarized photon is guided through an aspheric lens (L4) into a single mode fibre that consists of a nonpolarizing beam splitter (FBS) with 50% transmission and 50% reflection (50/50). The reflected photons enter part (b), where a multimode fibre beam splitter (MFBS 50/50) guides the light to SPCM2 and SPCM3. The transmitted photons enter part (c), where the light from a single mode fibre is collimated by a lens (L5) and directed towards a 50/50 beam splitter (BS), mirror (M) and object. Finally, an imaging lens (L6) images an object plane to the detector plane (dashed lines). In the detection plane is a second multimode fibre beam splitter (MFBS 50/50) attached to a two-dimensional motorized linear translation stage (XY) and connected to the SPCM4 and SPCM5.

First, the laser light at 405 nm illuminates a 10 mm long periodically poled potassium titanyl phosphate (ppKTP) nonlinear crystal (Raicol Crystals Ltd, 10 µm periodic poling), generating photon pairs at 810 nm in the process of collinear type-II SPDC. The orthogonally polarized photon pairs are separated into two beams by a polarizing beam splitter. The vertically polarized photons are guided through a fibre to SPCM1, which registers the signal used to herald single

photons. The horizontally polarized photons are led either to setup in the front of the interferometer or to the interferometer. Objects (a silver mirror with a laser written pattern and a cover glass positioned on the dielectric mirror) are placed in one of the optical arms of the interferometer. In the second arm of the interferometer, a mirror M is placed on a one-dimensional motorized translation stage. The interferometer arms were matched by moving the mirror before hologram acquisition. After the interferometer is an imaging lens that constitutes the image plane Michelson interferometer that is used for the hologram recording. For the hologram acquisition, a multimode fibre attached to a two-dimensional (XY) motorized linear stage and coupled to the single-photon detectors was used. The single-photon states can be characterized with the two single-photon detectors in front of the interferometer.

The fundamental interference fringes are introduced by tilting the two, object and reference beams with respect to each other. The hologram image is sampled on the fly and line-by-line, where the acquisition of the line always starts on the same side of the raster scan path. The pixel size is determined as a product of the stage velocity and integration time. All holograms are recorded with a pixel size of 30 microns. The time tagging module (time-to-digital converter) is used for data collection.

3.4. Experimental challenges

3.4.1. Laser and down conversion source

According to the specifications, the diode laser (Integrated Optics UAB, 405 nm SLM Laser, VBG Diode, PM fibre) emits light in the continuous-wave regime at 405 nm with a power of 18 mW and a spectral line width (FWHM) of 0.1 pm. The stable single-frequency regime is achieved through the use of a volume Bragg grating with temperature stabilization (in our case at 28°C) and automatic power control. However, the single frequency is guaranteed only at the default settings. PBS inside the laser ensures good polarization contrast. The spatial profile is Gaussian due to direct coupling into polarization-maintaining fibre. Over time, the power of the laser gradually decreased to only 1 mW. The main suspect of the reduced power was misalignment of internal optical elements. Later discussion with the manufacturer [72] identified that the problem was connected to the humidity that affects the glue used for positioning optical elements (according to the manufacturer, the new lasers should be now without this defect). The humidity- and temperature-dependent thermal expansion/contraction

of the glue misaligned the optical elements. The problem was reduced by using an additional thermoelectric module and temperature controller so that the laser was heated to constant temperature (26°C) below the laser diode operating regime. This solution seems to reduce the humidity inside the laser without any additional service. The power of the laser was raised to a more reasonable power of 8 mW. By carefully aligning the positions of the optical elements (independent of laser), care was taken to prevent any back-reflections that could damage or disrupt the laser diode.

As a source of down conversion photon pairs, a 10 mm long nonlinear ppKTP crystal type-II was used. To maintain the low cost and efficiency of the coupling system, a colinear nonlinear type-II crystal with standard periodic poling seems to be a reasonable choice. The potential risk with this type of crystal (with a standard mask used for periodic poling) is that a slightly (to an order of 0.1 nm) wrong pump wavelength and poling period accuracy (to an order 0.1 μm) could mean that the crystal should be cooled down below room temperature to produce degenerate photon pairs. Cooling down the nonlinear crystal could cause a condensation problem like in Ref. [73]. An appropriate laser pump wavelength and nonlinear crystal were acquired. Another important issue was fluorescence coming from optical elements. Fluorescence was reduced to a minimum by careful choice (e.g., fused-silica optics for pump wavelength) and testing of various optical elements (e.g., spectral filters). For example, even the most renowned bandpass filter in certain cases showed some fluorescence in certain cases. Fluorescence can induce a devasting effect for the detection of photon pairs generated in the down conversion crystal.

The laser beam was collimated with a short aspheric lens (focal length of 4 mm) and weakly focused with a plano-convex lens (focal length of 300 mm). The SPDC beam was collimated with another plano-convex lens (focal length of 400 mm) and coupled with an aspheric lens (focal length of 11 mm) into a single mode (HP780) patch cable. Reasonable coupling efficiency (heralding efficiency of approximately 30% with the SPCMs) was achieved with a beam walking procedure based on two mirrors, fine alignment of the focal distance (Z-axis) for the coupling lens, and alignment of XYZ for the focusing and collimation lenses. In this way, the acquisition of an expensive high-precision XYZ flexure stage has been avoided.

Figure 7 shows the experimental realization of the down conversion source in the laboratory. Due to the coupling of down conversion photon pairs into fibre, it is easy to transfer the photon pairs to another optical breadboard where the characterization setup and the interferometer are

positioned. Most of the shown optical posts and clamps were made at the Institute's machine shop.

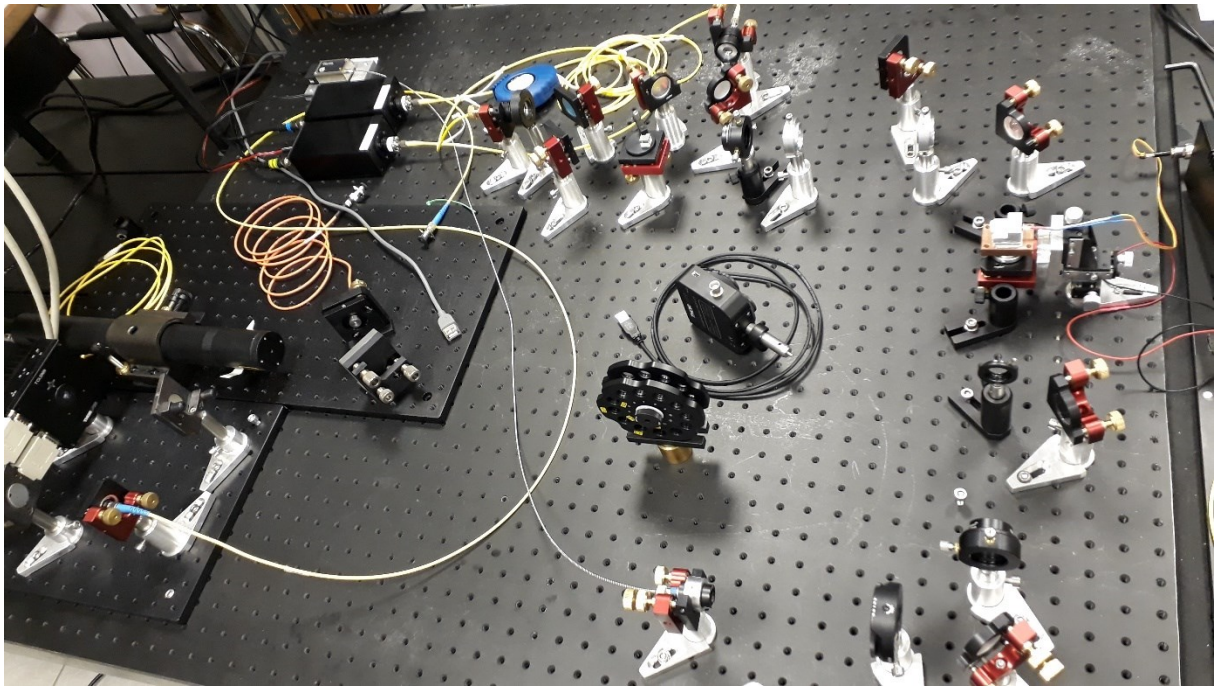

Figure 7. The experimental setup for the generation of down conversion photon pairs. The laser beam emerges from the polarization maintain fibre at the bottom middle part of the figure. In the top left corner, two SPCMs (black boxes) with a single mode fibre (yellow) and laser (matchbox size) with a 1 m long polarization-maintaining fibre (gray metal enclosure) are shown. The alignment laser (at 810 nm) coupled into a single mode fibre is positioned on the small square optical breadboard. Previously, the Helium Neon laser positioned on the rectangular optical bread was used as the alignment laser. The Helium Neon laser is convenient to use due to beam in visible spectral range. However, the wavelength mismatch between the SPDC beam and the Helium Neon laser beam leads to different propagation due to different indices of refraction for different wavelengths.

To tune the temperature phase matching of the ppKTP crystal, an oven with a temperature controller was designed and built. The design was based on a thermoelectric (Peltier) element, platinum resistance (PT100) thermometer and precise readout of voltage with a nanovoltmeter that was proportional to the temperature on the sensor near (0.1 mm to) the crystal. The measured temperature stability was 0.01 K. The type-II nonlinear crystal used is relatively robust to temperature changes (0.2 nm/K), and the 3 nm bandpass filters used do not impose strict conditions on the temperature changes. However, precise tuning of the temperature can

be advantageous in certain cases. Adjustment of the temperature is possible with (an analogue) knob with a marked scale. This part of the setup is shown in Figure 8.

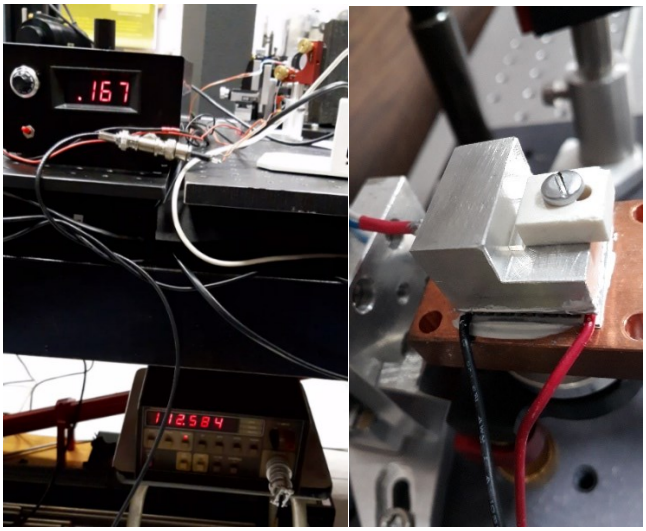

Figure 8. Home-built temperature controller (black box), nanovoltmeter (below optical table) with wires leading to the oven with 10 mm long nonlinear crystal (shown on the right).

3.4.2. Interferometer

The alignment of the modified Michelson interferometer was a challenging task due to the low coherence length of the SPDC photon pairs and angular deviation of the motor translation stage (Thorlabs PT1-Z7). The latter was improved by the usage of a better linear motor translation stage (Newport DL225 Delay Line Stage). To align the interferometer, a bucket detector was positioned behind the interferometer that measured the total intensity. The perfect constructive interference at the output of the Michelson interferometer was found for the maximum count rate on the bucket detector. Later, the positions of mirrors were aligned to obtain diagonal interference fringes which were used for imaging the objects. Different objects have been tested for recording of the holograms. However, the main results were shown with laser written pattern on the silver mirror and a modified Michelson interferometer with the cover glass positioned on the horizontal dielectric mirror. Remark that the most challenging is to maintain the interferometer stability during the long acquisition time (up to 72 h) of the hologram. For passive stabilization of the interferometer, a careful selection of similar optomechanical elements with the same coefficients of thermal expansion has been made, and attention to the

compact size of the interferometer has been given. Two interferometer configurations are shown in Figure 9.

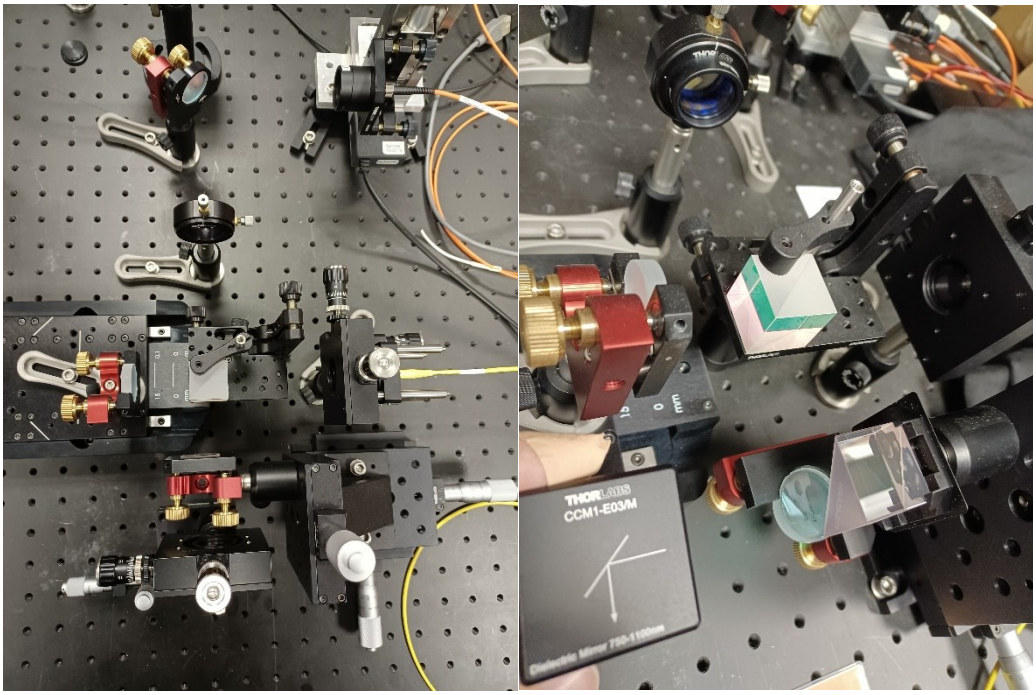

Figure 9. Twyman-Green interferometer setups with imaging lens behind the interferometer. In the left configuration, the object is vertically positioned, and in the right configuration, the object is positioned horizontally.

3.4.3. Detection and acquisition system

A type-II nonlinear crystal gives orthogonal polarized photon pairs. This fact can be used to split photon pairs with a polarised beam splitter. When the photon pairs are separated, one can be used as a trigger photon; that is, the detection of the trigger photon can herald the other so-called signal photon. For the detection of single photons, a homemade [74] and commercial [75] single-photon avalanche photodiodes were used. Due to achieving a perfect spatial profile used for imaging, single mode fibre has been preferred. For the final coupling of the beam after the interferometer, a multimode fibre was preferred due to the large core size, i.e., larger collection efficiency. Another advantage of the fibre systems is that it is easy to change the position of fibre beam splitters used for characterization of the light source at different places. Furthermore, by removing and adding the fibre beam splitter, optimization of the photon count rate is possible.

Homemade single photon counting modules are based on single-photon avalanche photodiodes SAP500 manufactured by Laser Components and commercial single photon counting modules are manufactured by Excelitas. According to the typical specifications [75], the silicon avalanche photodiodes used have a single-photon detection efficiency with a typical peak efficiency of 65% at 650 nm (Excelitas SPCM-AQRH-11-FC, Excelitas SPCM-AQRH-12-FC), and the homemade [74] avalanche photodiodes are slightly less efficient. The detection efficiency at 830 nm is typically 45%, so that at 810 nm a bit higher efficiency than at 830 nm is expected. The single photon timing resolution is limited by the detector jitter, which is typically 350 ps. Typical dead time of the detectors is around 22 ns. The dark count rate of detectors ranged from slightly below 500 cps to 5000 cps. The manufacturer specified variation in the average dark count rate at 5°C to 70°C is ±20%, and the variation in the average dark count at constant temperature (6 hrs at 25°C) is ±10%. Obviously, the measurements can be influenced by the ambient and surrounding conditions. Later, results for the measurement of the dark count rates of the detectors are presented in section 4.2.

At the beginning of the research, a homemade coincidence circuit was made, and a commercial frequency counter (Stanford SR620) was used for the measurement of coincidences. The coincidence time window was limited to the pulse width coming from the detector, and the delays were estimated from the measurement of the optical path and patch optical fibre and matched by the proper length of coaxial cables. At the later stage, this method was changed due to the acquisition of a time tagger module (Swabian Instruments, Time Tagger Module 20) with much more advanced features, such as time stamping with 80 ps time resolution, arbitrary size of the coincidence time window, and with digital resolution of 1 ps. The single photon counting modules based on silicon avalanche photodiodes are shown in Figure 10 and the time tagger module is shown in Figure 11.

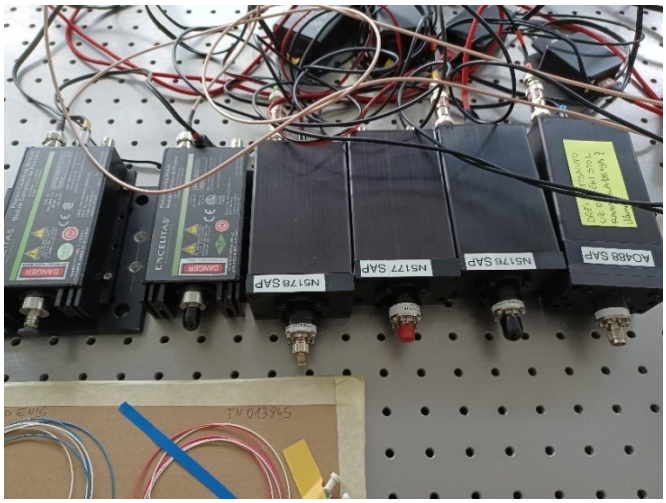

Figure 10. Single photon counting modules with FC adaptors used in the experiments.

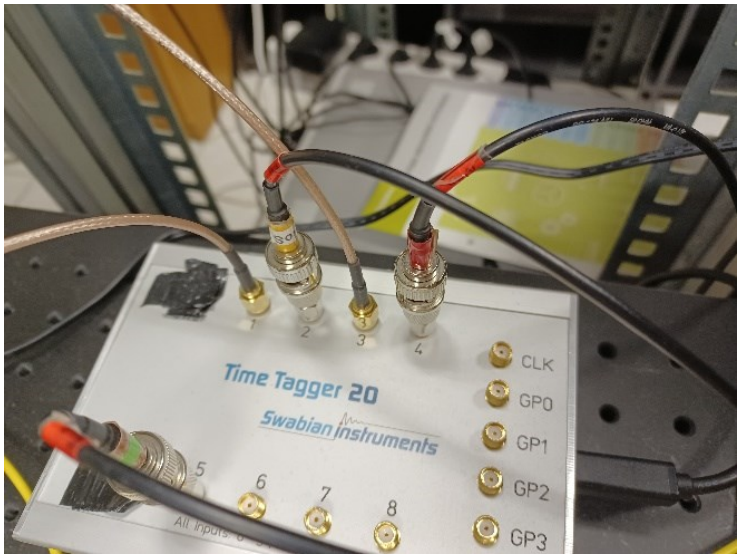

Figure 11. Time tagger module with coaxial cables connected to single photon counting modules (shown in Figure 10). Note that the LEDs are covered with black tape due to influence on the count rate of the detectors. All the sources of light in the laboratory were covered, including from the floor of a slightly elevated laboratory door.

Programs for setting parameters and acquiring the signal were written in LabVIEW software. Figure 12 shows a front panel of the LabVIEW program. The hologram image is obtained by on-the-fly and line-by-line scanning, with line acquisition always starting on the same side of the raster scan path. The pixel size in the x dimension is equal to the product of the stage velocity (v_x) and the integration time (Δt), $\Delta x = v_x \cdot \Delta t$. The pixel size in the y dimension is made the same size by moving each consecutive line by $\Delta y = \Delta x$. All the detection channels are connected to time tagging module (TTM).

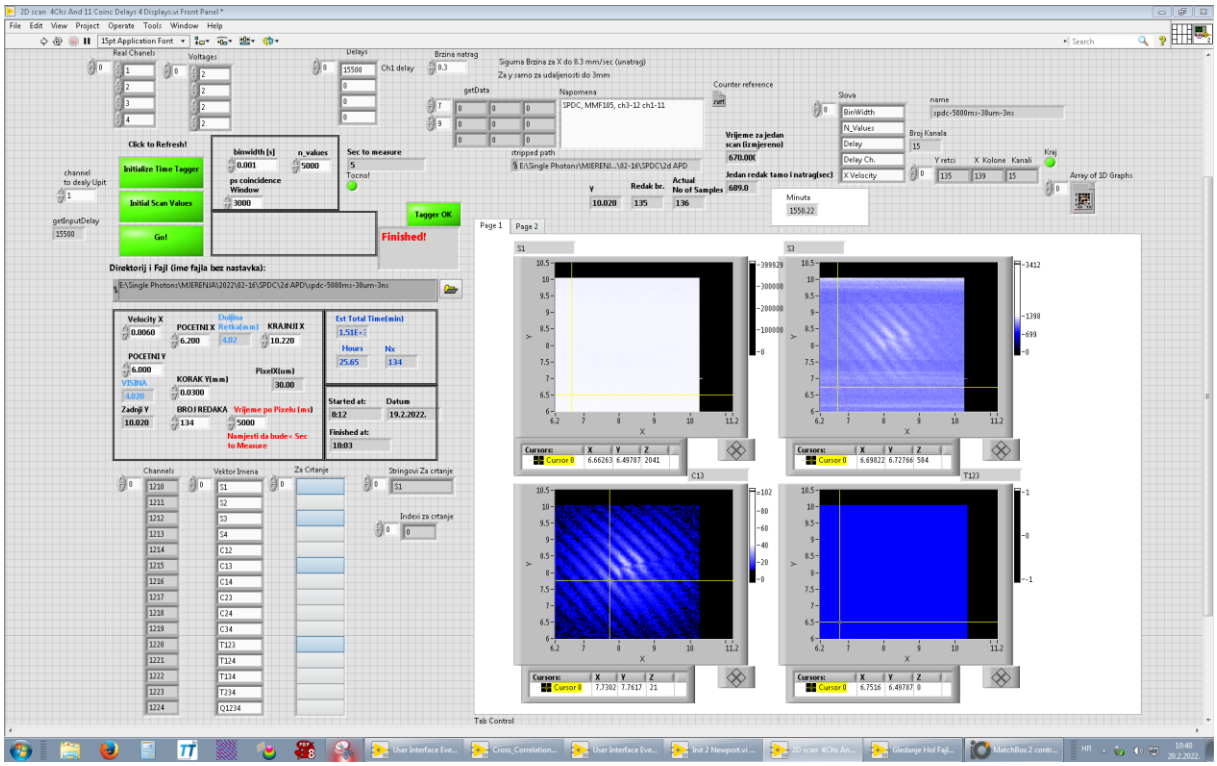

Figure 12. LabVIEW program for setting parameters and acquisition of the signal with a two-dimensional motorized translation stage and multichannel acquisition system of the signal from the SPCMs.

4. Results: light source, light-sensitive detectors, and holograms

4.1. Single-photon source

4.1.1. Second order correlation function

Before recording holograms, I characterized $g^{(2)}(0)$ using SPCM1 as a heralding detector and dielectric mirror instead of the first FBS 50/50 shown in Figure 6. In this way all the light goes to SPCM2 and SPCM3, which are now heralded detectors. In Figure 13 (upper inset), the measurement of the second order correlation function clearly demonstrates the single photon character of the implemented light source over 24 hours. The final value of the second order correlation function, $g^{(2)}(0) = 0.00440(1)$ is among the best recorded compared to the literature [76]. The $g^{(2)}(0)$ uncertainty error is small due to the accumulation of events over a long time. The error is determined by applying the Poisson distribution to the count rates. Measurement of the second order correlation function for a single SPDC arm gives $g^{(2)}(0)_{nh} = 1.00115(107)$ and it is also shown in Fig. 3 (lower inset). This result agrees with the literature [52] and illustrates the difference between the photon statistics associated with heralded single-photon states and non-heralded light from SPDC. These two different natures of light, obtained from same SPDC source have been used for simultaneous recording of two holograms with continuous monitoring of photon statistics.

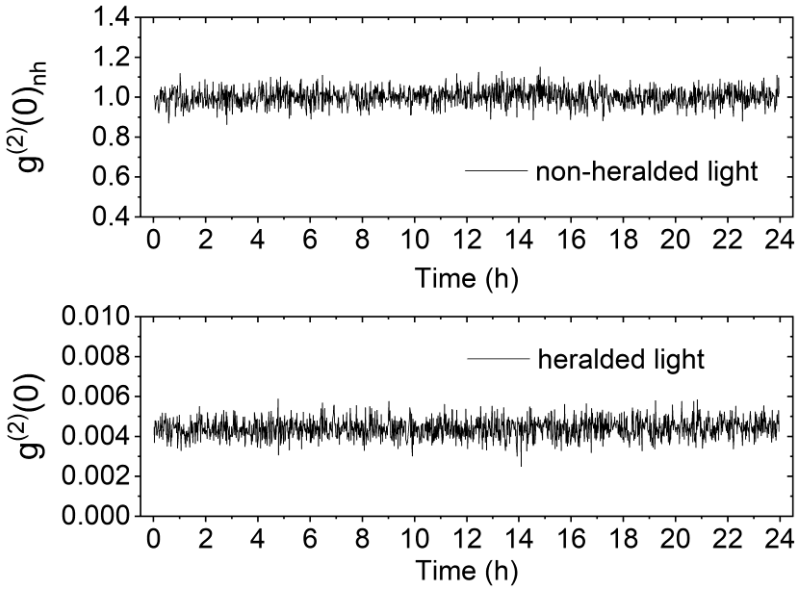

Figure 13. $g^{(2)}(0)$ and $g^{(2)}(0)_{nh}$ measured through 24 hours. Black line represents value of $g^{(2)}(0)$ and $g^{(2)}(0)_{nh}$ for measurements collected every minute. Note the different vertical scale on the two graphs.

When recording holograms in the setup shown in Figure 6**,** the light source is monitored before the interferometer by SPCM2 and SPCM3 and after the interferometer by SPCM4 and SPCM5. The measurement of $g^{(2)}(0)$ made with the characterization setup in front of the interferometer (SPCM2 and SPCM3) during the recording of the holograms shown in Figure 21 gives $g^{(2)}(0) = 0.00721(3)$. The difference between the two observed values of $g^{(2)}(0)$ is due to losses introduced by the additional fibre beam splitter and possible small alignment changes of the pump source during the two different experimental trials. The triple coincidence between SPCM1, SPCM4, and SPCM5 is zero due to the low photon count rates at SPCM4 and SPCM5. Figure 29 shows hologram recordings and the zero triple coincidences. The photon counts are low because the photons are spread over the detection image plane. Because of these low count of photons, $g^{(2)}(0)$ cannot be explicitly stated, but this also indicates a single-photon nature of light at the image detection plane. These results of $g^{(2)}(0)$ measurement are fully consistent with the proposed single-photon generation and detection protocol for recording non-classical holograms. Examples of recorded holograms and their reconstructions are shown in section 4.3**.**

4.1.2. Spectral characterization of spontaneous parametric down conversion

The spectral distribution of the SPDC in the ppKTP nonlinear crystal depends on the crystal temperature and pump of the laser. The temperature dependence of the spectral distribution of the collinear type-II ppKTP nonlinear crystal with a length of 10 mm and an aperture of 1 mm x 2 mm was measured by coupling light into the fibre, leading to a spectrograph (Andor Shamrock SR301i with holographic grating with 1800 lines/mm) and CCD (Andor iDus420A with 26 µm · 26 µm pixel size), as specified below in Figure 14. Figure 15 shows a typical result of the measurements of the spectral distribution of the SPDC. From the fit, it is visible that the peak centre wavelength changes as expected to be ≈ 0.2 nm/K.

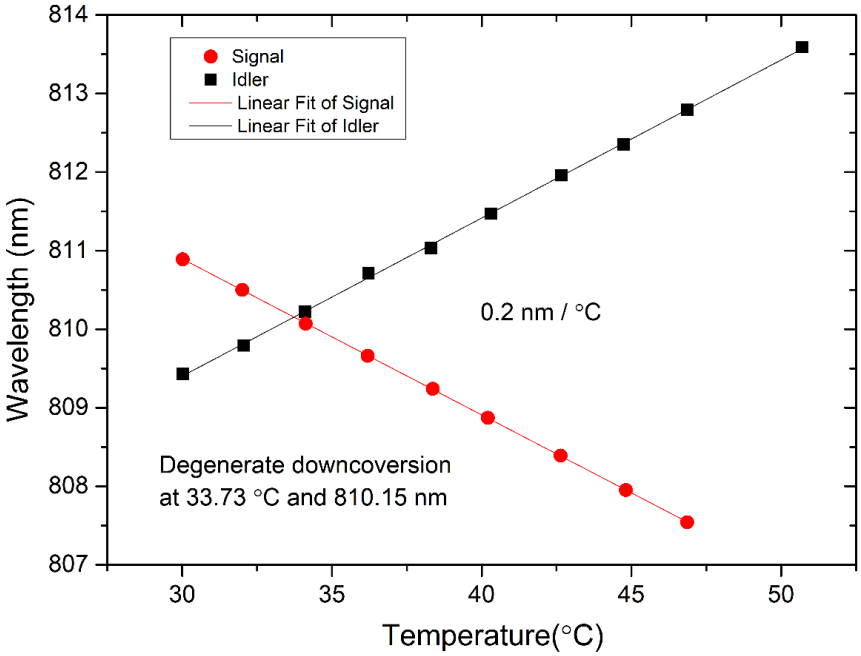

Figure 14. The change in the peak centre wavelength of the photon pairs is shown as a function of crystal temperature.

The spectral profile of down-converted photons for only one polarization near the degenerate wavelength is shown in Figure 15. The *sinc* profile is not clearly visible due to noise. The polarization can be simply selected by using a polarizer. The FWHM (0.59 nm) is close to the expected value (0.55 nm) for this type and length of crystal. The difference between the values could be due to systematic error. The wavelength resolution according to the spectrograph specifications is limited <0.2 nm and accuracy ±0.2nm.

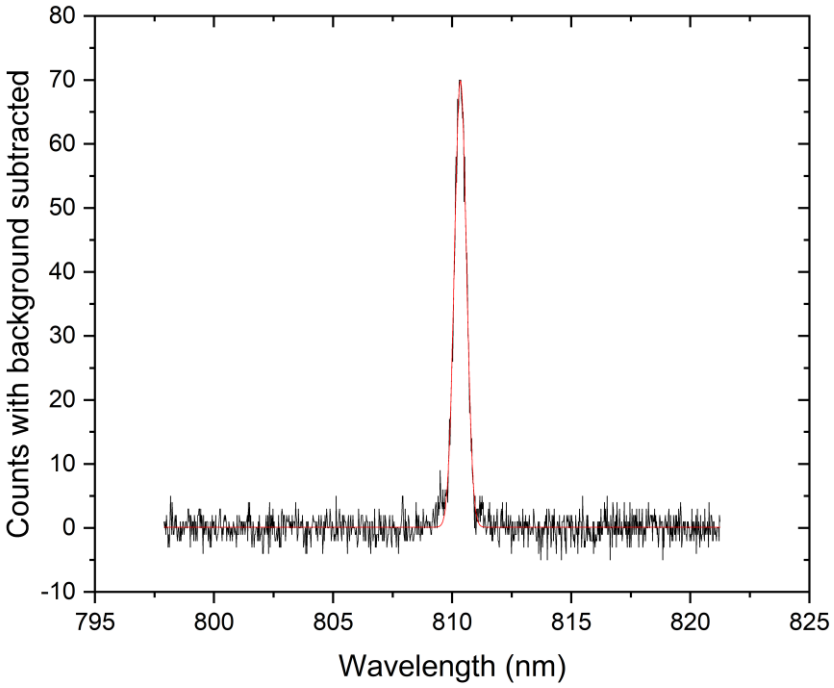

Figure 15. The spectral profile of the down-converted photons for a selected polarization. The data (black) are fitted to Gauss function (red) and the result is a central wavelength of 810.34 nm and a FWHM of 0.59 nm.

4.1.3 Michelson fringes

As seen from measurements in the previous section (4.1.2), the SPDC source has a relatively broad spectrum, i.e., a short coherence length. Therefore, to have high visibility of interference fringes, it is critical to perfectly align the Michelson interferometer. The Michelson interferometer is aligned (balanced) when the two arms of the interferometer have equal lengths. Maximum oscillations in the amplitude occur for positions near perfectly balanced arms of the interferometer. This fact can be used for the perfect alignment of the interferometer. Before proceeding to alignment at the single photon level, perfect overlap between two beams emerging from two arms of the interferometer was found with the CCD and alignment laser at 810 nm.

Measurement of Michelson fringes for different displacements of a mirror in one of the arms of the interferometers is performed by collecting all light from a single output behind the

interferometer without the imaging lens (shown in Figure 6). The light is collected by a multimode fibre with an attached aspheric lens. The fibre leads the light of the SPCM detector.

Figure 16, Figure 17 and Figure 18 show the photon count rate for different positions of the mirror moved by the motorized translation stage. The upper and lower envelopes for recording with single-photon states in Figure 16 and with non-heralded light in Figure 17 are symmetric. The shape of fringes is visible in Figure 18 with a finer X-scale. For the Gaussian spectral distribution, the coherence length can be obtained from $l_c \approx \lambda^2 / \Delta\lambda$. For the FWHM of 0.55 nm (at a central wavelength of 810 nm), this leads to $l_c = 1119 \mu m$, which agrees well with the coherence length obtained from interferograms (shown in Figure 16 and 17). Notice that the movement of mirror accounts for twice the displacement as the light travels to the mirror and back, so the shown FWHM should be multiplied by two to get the coherence length. The difference between the values is probably due to the errors in determination of the exact position of the stage.

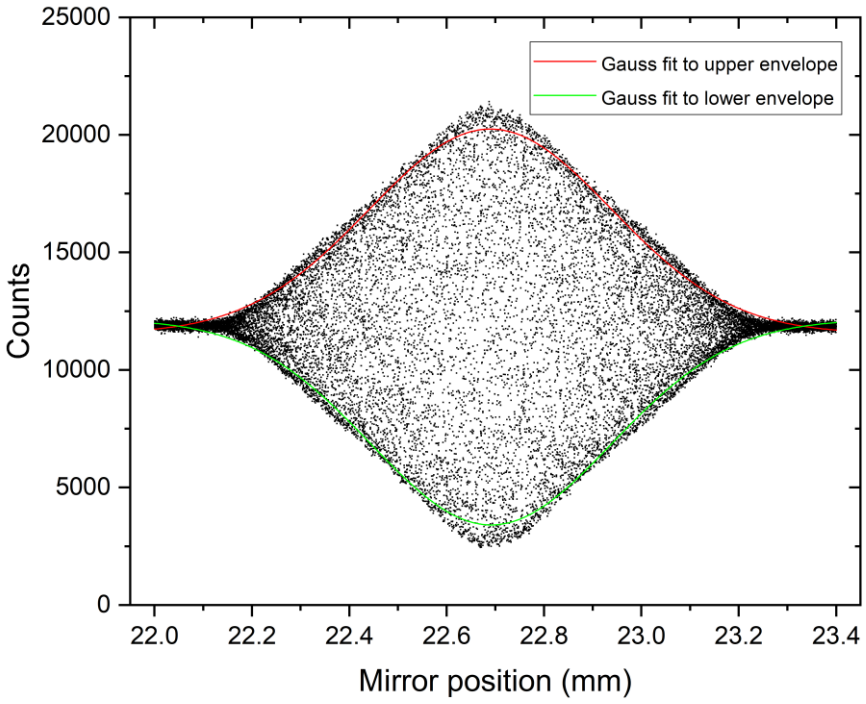

Figure 16. Michelson fringes with single-photon states as path difference varies. FWHM of upper envelope is 0.587 mm and of lower envelope is 0.582 mm.

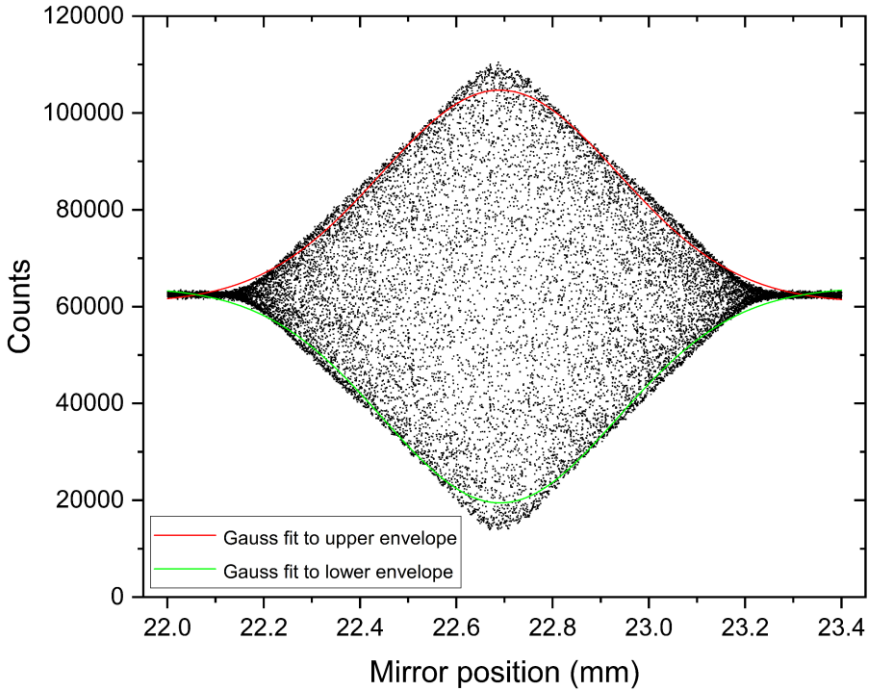

Figure 17. Michelson fringes with non-heralded light as path difference varies. FWHM of upper envelope is 0.581 mm and of lower envelope is 0.575 mm.

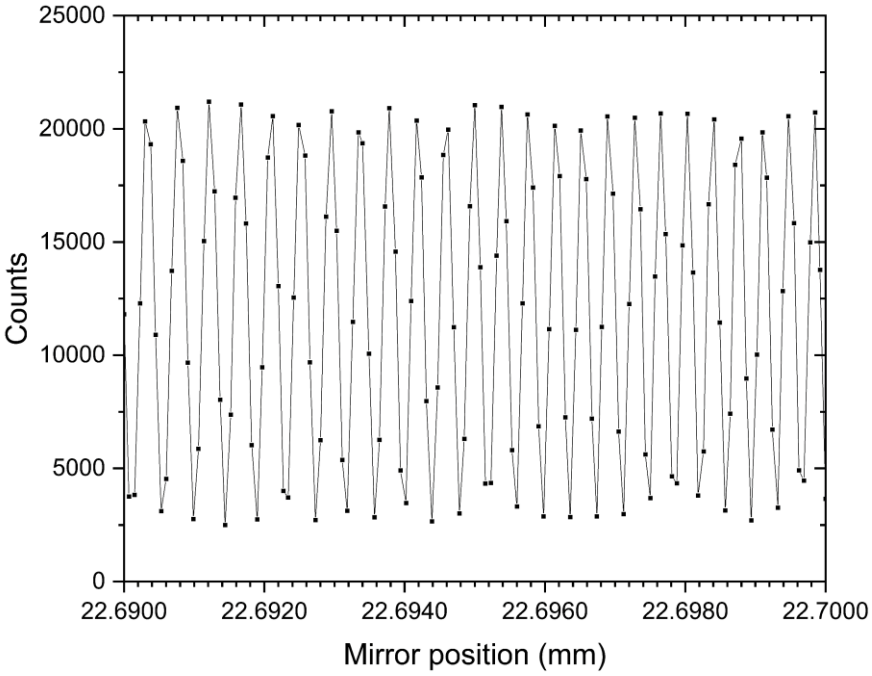

Figure 18. Visible Michelson fringes with single-photon states as path difference varies on a shorter interval than in Figure 16 and 17.

4.2 Noise of single-photon avalanche photodiodes

The purpose of the long run measurements of the dark count rate is to test the stability of the dark counts of the single photon detectors. These results were used in the quantitative evaluation of the hologram recordings. Figure 19 shows typical results of the long run measurements of the dark noise of the single-photon avalanche photodiodes used in this work. The measurement was performed with four detectors simultaneously for 24 hours. The results were collected every 5 s.

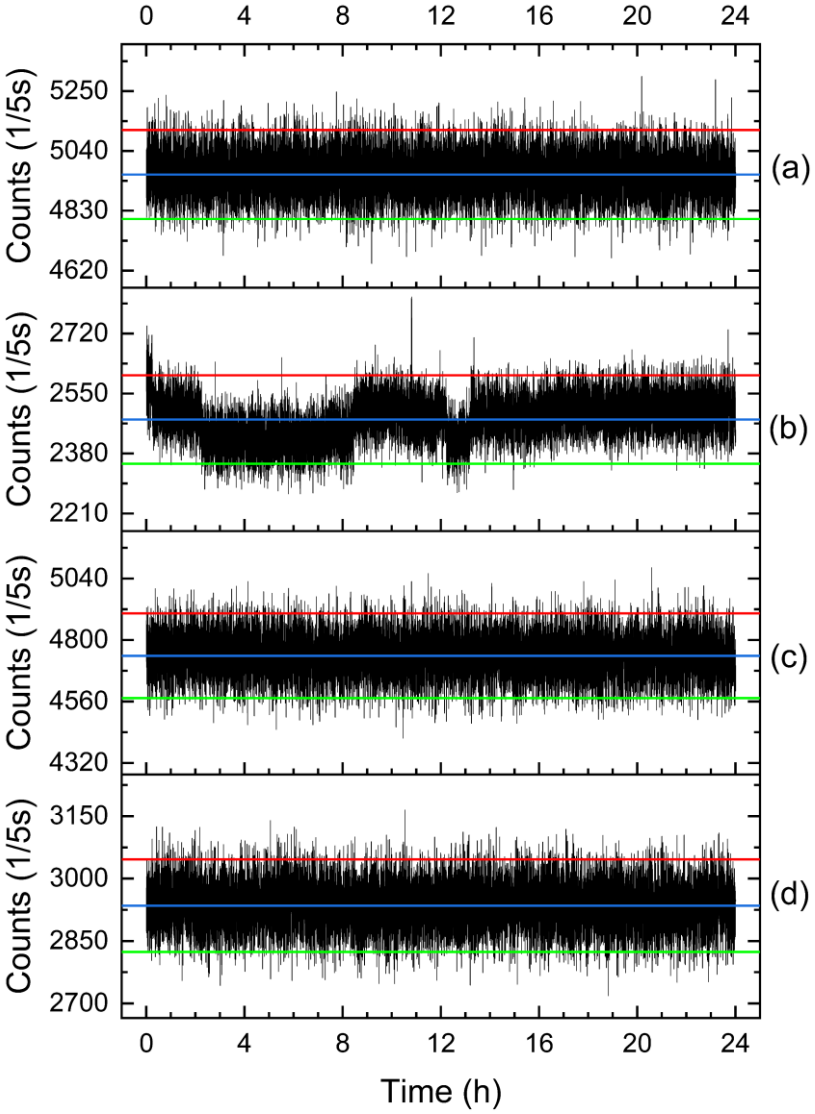

Figure 19. Dark counts for four single photon avalanche photodiodes: (a) Homemade no. 78, (b) Excelitas SPCM-AQRH-12-FC, (c) Homemade no. 76, (d) Excelitas SPCM-AQRH-11-FC. Data measurements (black line), mean dark counts (blue line), upper two standard deviations (red line) and lower two standard deviations (green line).

In principle, the dark count follows a Poissonian distribution. However, it is known that there can exist some variability of the mean dark count rate [75]. The variability of the mean dark count and some abrupt changes have been observed. In particular, Figure 19 (b) shows abrupt changes (± 2 standard deviations) in dark count for a longer period of time (h). The variation of dark counts can be considered as a measure of the stability of the average dark count of the specific module.

More quantitative measures that describe Figure 19 are shown in Table I. For example, when making comparison between two commercial detectors, it is visible that the detector with the lower count rates has larger fluctuations in dark count (quantified in terms of standard deviations) than the detector with higher mean dark count. Similar results have been obtained for comparison between two homemade detectors. This is consistent with the manufacturer's datasheet [75] and the discussion provided in section 3.4.3. These dark count fluctuations can strongly influence the measurements when the acquisition time is long.

Counts (1/5s)	Homemade no. 78 Figure 19 (a)	SPCM-AQRH-12 Figure 19 (b)	Homemade no. 76 Figure 19 (c)	SPCM-AQRH-11 Figure 19 (d)
Mean (blue line)	4957	2476	4739	2935
+2 SD (red line)	5035	2539	4905	3047
-2 SD (green line)	4879	2413	4573	2823
Max	5302	2824	5083	3046
Min	4646	2266	4417	2719
SD	78	63	83	56
Poissonian SD	70	50	68	54

Table I. Count rates for the four single photon counting modules. SD is standard deviation and Poissonian SD is standard deviation attributed to Poissonian process (random generation of dark counts) which is equal to the square root of the mean.

When imaging in low-light conditions the fluctuations of the dark count rate may be higher than the signal. In this way, object visibility can be buried in the dark noise of the detector. A cost-effective solution to reduce the noise of the detection system could be to use trigger events so that the detector only detects events when signal photons are expected to arrive. The results of this method are demonstrated in the following section 4.3.

4.3 Objects, holograms, and reconstructions

For the demonstration purpose, I used two different input objects: a silver mirror with a laser written pattern (amplitude object) and part of a microscope cover glass (phase object) positioned on the dielectric mirror. Figure 20 shows both objects. Depending on the object, two experimental configurations of the interferometer were used, one for positioning the object in the horizontal plane and one for positioning the object in the vertical plane (see section 3.4.2. for more details).

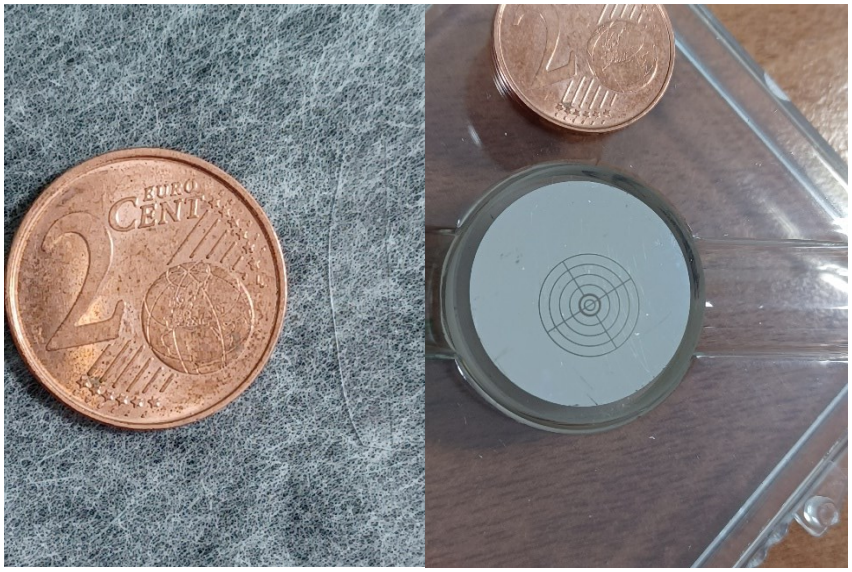

Figure 20. Left: part of a microscope cover glass; and right: silver mirror with a laser written pattern. The two-cent coin is used as an illustration of the size of the objects.

As the first object in the interferometer I use, the silver mirror with laser written pattern. The object is vertically (see Figure 9: left) positioned in the mirror mount for Ø1" optics. In the middle of the laser written patterns are two half circles. The holograms recorded with single-photon states and with non-heralded light are shown in Figure 21 (a) and (e), respectively. Next to the holograms, their amplitude and phase reconstructions are shown. In the case of the reconstructions corresponding to heralded light, the two half circles are clearly distinguished from the non-reflective background. However, the object is not visible from the hologram recorded with non-heralded light. In other words, the amplitude and phase reconstructions obtained from holograms recorded with single-photon states show clear advantage over the reconstructions obtained with non-heralded light.

The amplitude reconstructions correspond to the amplitude part shown in Equation (23), the phase reconstructions to the phase part of the same Equation (23), and the phase corrected

reconstructions correspond to the phase part shown in Equation (27). All reconstructions obtained with heralded single photons and with non-heralded light use the same reconstruction parameters, i.e., the same area is used for extraction of the first diffraction order and the same linear phase correction.

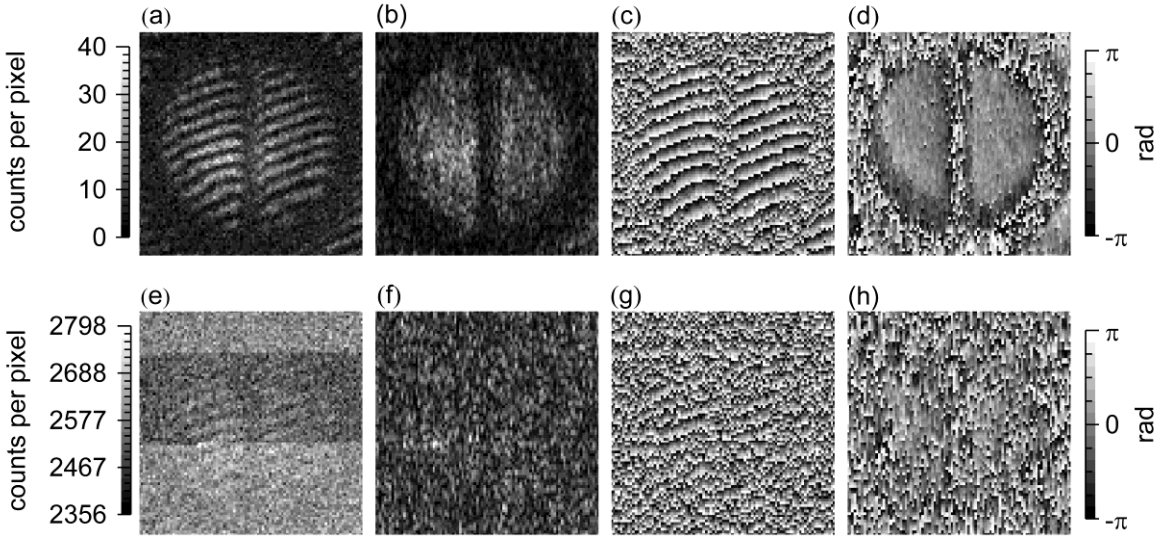

Figure 21. Upper row**:** a hologram recorded with heralded single photons (a); the corresponding amplitude (b); phase reconstruction (c); phase corrected reconstruction (d). Lower row: a hologram recorded with non-heralded light (e); the corresponding amplitude (f); phase reconstruction (g); phase corrected reconstruction (h). Recordings are 93x85 pixel, the integration time is 5 s / pixel and the coincidence time window is 2 ns.

Quantitatively, the quality of the hologram fringes is derived from the standard definition of visibility,

$$V = \left(N_{max} - N_{min}\right) / \left(N_{max} + N_{min}\right) \tag{48}$$

, where N_{max} is the local maximum and N_{min} is the next local minimum to maximum. For evaluation of the visibility, a line near the beam centre of the hologram recorded with heralded and non-heralded light was chosen. The profile of the line is shown in Figure 22. The line corresponds to the vertical line taken on the horizontal pixel number 39.

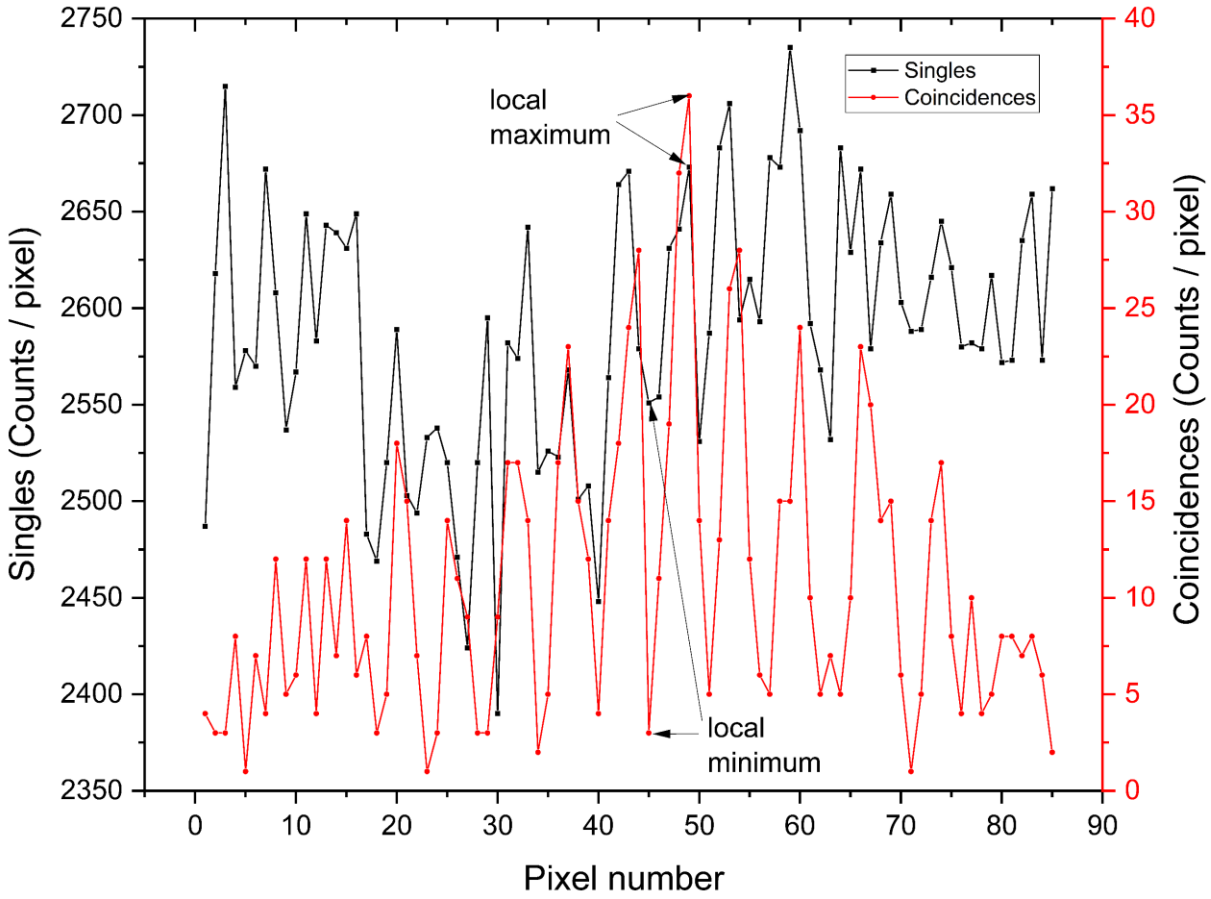

Figure 22. The profile of single line taken from holograms (Figure 21) recorded with heralded light (coincidences) and with non-heralded light (singles).

The visibility near the beam centre of the hologram recorded with non-heralded light is 2(1)%, and with single-photon states is 85(8)%. The complete results used to calculate visibility of the fringes are shown in Table II. The hologram recorded with non-heralded photons has low visibility due to predominant noise of the detector in comparison to signal from the interferometer. The dark noise of the detector is 2476(63) counts/ (pixel · 5 s), and it agrees with the (local) minimum that is shown in Table II. Overall coincidence noise calculated according to Equation (43) for the later shown hologram in Figure 21(a) is 5(2) counts, and it is also in agreement with the (local) minimum. Spatial variations of visibility are predominantly due to properties of the object and the small, non-perfect and non-uniform Gaussian beam profiles of two overlapping beams that form the fundamental interference fringes, or, in other words, due to the decrease of intensity and spreading of illumination from the beam center. Depolarization of the beam entering the interferometer as well as depolarization effects inside the interferometer, for example due to the object may also influence the visibility. As can be seen in Table II, the maximum should be increased to 30612 counts / (pixel · 5 s), to achieve

the same visibility as for the heralded single-photon states without changing the count rate at the minimum (obtained with non-heralded light). In other words, by assuming the same minimum, the maximum should be increased 850 times more than it is used in the case of single-photon states.

Table II. Average counts / **(**pixel· 5 s) for a line in recorded holograms (Figure 21(a) and (d)) and their visibilities.

	Single-photon states	Non-heralded light
Maximum	36(6)	2673(52)
Minimum	3(2)	2551(51)
Visibility	85(8)%	2(1)%

For a more quantitative description of the overall quality of the hologram, I calculated and compared the directly measured and estimated SNRs according to the model presented in Section 2.8. In summary, directly measured SNR is calculated according to Equation (42) for the heralded technique and according to Equation (45) for the non-heralded technique. I do not consider the background noise separately from the dark noise, because detectors cannot distinguish between these two sources of noises, and I took special care to remove possible background noise due to stray light.

The dark region of the hologram recorded with single-photon states consists of pixels with the counts ≤7 and the rest pixels (counts >7) are defined as the bright region of the hologram. This threshold value was chosen because it agrees well with the estimated coincidence noise, separates well the bright region from the dark region, and finally gives the best agreement between the measured and the estimated SNR. Due to much lower noise in the hologram recorded with heralded photons compared to non-heralded, I determine whether the pixel belongs to the bright or dark region from the hologram recorded with heralded single-photon states. Masks associated with bright (mask covering dark region) and dark region (mask covering bright region) are shown in Figure 23. The estimated noise is obtained from measurements of SPCMs dark count. The estimated coincidence noise for hologram recorded with single-photon states can be calculated from the bright region according to Equation (43), where the average count on the imaging detector N_I = 2579(65) counts / (pixel · 5 s), the average count on the trigger detector N_T = 955018(7879) counts / (pixel · 5 s), the average dark count of the imaging detector N_{DI} = 2476(65) counts / (pixel · 5 s), the average dark count of the

trigger detector N_{DT} = 2935(56) counts / (pixel · 5 s) and the coincidence time window Δt = 2 ns. From this is visible that the last two terms cancel, because $N_I \approx N_{DI}$. The coincidence noise and the noise of the imaging detector are not subtracted in the holograms shown in Figure 21. The signal can be determined by subtracting the noise from registered counts. The data variability is stated as standard deviation.

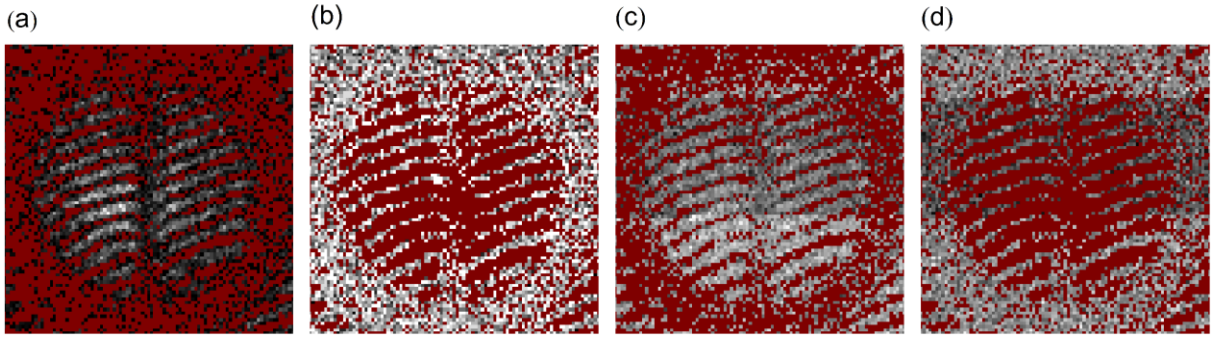

Figure 23. Holograms with masks used for separation between bright and dark region. Hologram recorded with heralded light: (a) shows bright region with mask covering dark region and (b) shows dark region with masks covering bright region. Hologram recorded with non-heralded light: (c) shows bright region with mask covering dark region and (d) shows dark region with masks covering bright region. Red pixels are associated with missing values and grayscale pixels are associated with values used for calculation of signal, noise and SNR for corresponding hologram.

The better contrast of holograms recorded with single-photon states is obvious from Figure 21 and quantitatively from Table III. Table III also shows excellent agreement between the measured and estimated SNR for the recordings with single-photon states and non-heralded light. After subtracting noise, the signal (coming from either the reference or the object arm) is 8 counts / 5 s for the heralded single photons and 11 counts / 5 s for the non-heralded photons. Despite the comparable signal level, the object is not visible with non-heralded light because the measured noise at the single-photon detector (2568 counts / 5 s) is more than 200 times larger than the signal with subtracted measured noise (11 counts / 5 s) for the non-heralded single photons. The visibility of the object for the non-heralded hologram can be easily lost due to the noise fluctuations of the imaging detector, which are much larger than the true signal. Therefore, for example, in Table III, the standard deviation of the signal with subtracted measured noise (92) is larger than the mean value (11) for non-heralded light. In comparison to non-heralded hologram recordings, the results show that nanoseconds coincidence time window used for recording holograms with heralded single photons results in much improved contrast.

Clearly, non-heralded holograms are more susceptible (especially for long acquisitions) to any changes (see for example the dark stripe in Figure 21(e) such as light source intensity fluctuations, detector noise, fluctuations of detector noise, and residual background light, due to the continuous acquisition of signal. Assuming the same detection efficiency and noise, the signal should be increased to 4109 counts / (pixel · 5 s) to achieve the same SNR as for the heralded single-photon states. In other words, for the same minimum, the maximum should be increased 514 times more than it is used in the case of single-photon states.

Holograms from Figure 21	Single-photon states	Non-heralded light
Measured counts in bright region	13(5)	2579(65)
Measured counts in dark region	5(2)	2568(65)
Estimated noise	4.7(1)	2476(63)
Signal	8(5)	11(92)
SNR measured	2(1)	0.004(36)
SNR estimated	2(1)	0.004(37)

Table III. Average counts / pixel for the two recorded holograms (Figure 21(a) and (e)) and their SNRs. The number in the parenthesis is the value associated with one standard deviation.

The same object was recorded with slightly lower magnification so that a larger area of the object was captured. Holograms and their reconstructions are shown in Figure 24. In the reconstructions of amplitude and phase made from holograms recorded with single-photon states, the two half circles and the circle surrounding them are clearly visible, but with non-heralded light the object is almost invisible.

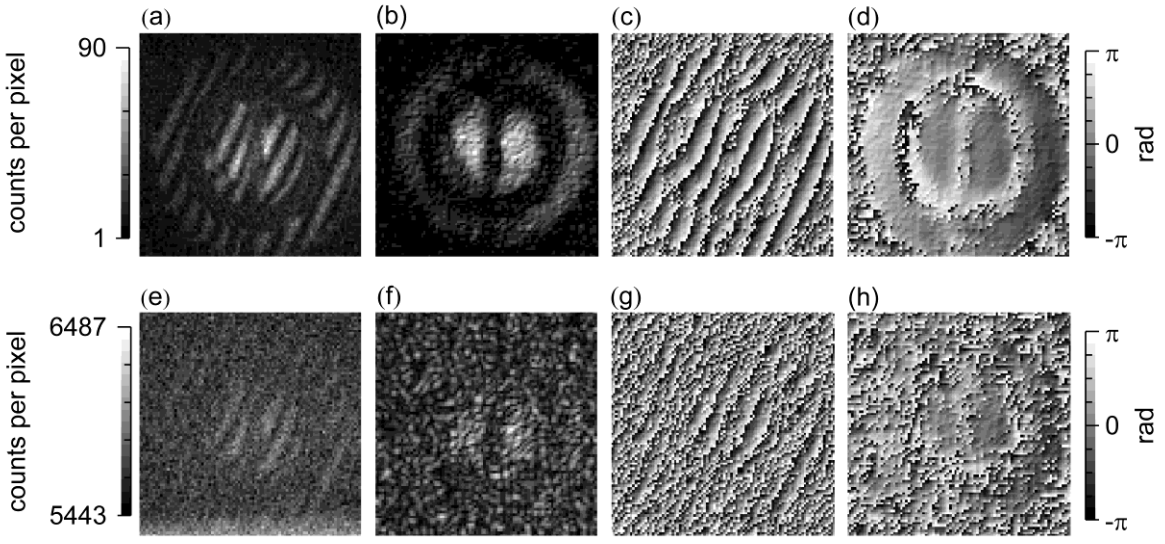

Figure 24. Upper row**:** a hologram recorded with heralded single photons (a); the corresponding amplitude (b); phase reconstruction (c); phase corrected reconstruction (d). Lower row: a

hologram recorded with non-heralded light (e); the corresponding amplitude (f); phase reconstruction (g); phase corrected reconstruction (h). Recordings are 91x92 pixel, the integration time is 5 s / pixel and the coincidence time window is 2 ns.

Quantitative results for Figure 24 using the previously defined measures, are shown in Table IV. For holograms shown in Figure 24, the average count rate on the imaging detector N_I =5772(159) counts / pixel, the average count rate on the trigger (heralding) detector N_T = 1 495 562(1689) counts / pixel, the average dark count of the imaging detector N_{DI} = 4957(78) counts / (pixel · 5 s), the average dark count of the trigger detector N_{DT} = 2935(56)counts / (pixel · 5 s), and the coincidence time window CTW =2 ns according to Equation (43) yields the estimated accidental coincidence noise CN=14.8(2). The agreement between measured and estimated values is good. Remark also that in the Table IV., the estimated noise for the detectors (column: non-heralded light) is different than in the previous measurement because another imaging detector with larger dark noise was used. Assuming the same detection efficiency and noise, the signal should be increased to 7923 counts / (pixel · 5 s) to achieve the same SNR as for the heralded single-photon states. In other words, for the same minimum, the maximum should be increased 440 times more than it is used in the case of single-photon states.

Holograms from Figure 24	Single-photon states	Non-heralded light
Measured counts in bright region	31(10)	5806(106)
Measured counts in dark region	13(4)	5772 (168)
Estimated noise	14.8(2)	4957(78)
Signal	18(10)	34(199)
SNR measured	1.4(9)	0.007(40)
SNR estimated	1.2(7)	0.006(34)

Table IV. Average counts / pixel for the two recorded holograms (Figure 24(a) and (e)) and their SNRs.

Masks associated with bright (mask covering dark region) and dark region (mask covering bright region) for Figure 24 are shown in Figure 25. The dark region for heralded light contains all the (estimated coincidence) counts per pixel ≤21 and bright region contains all the (estimated coincidence) counts per pixel >21.

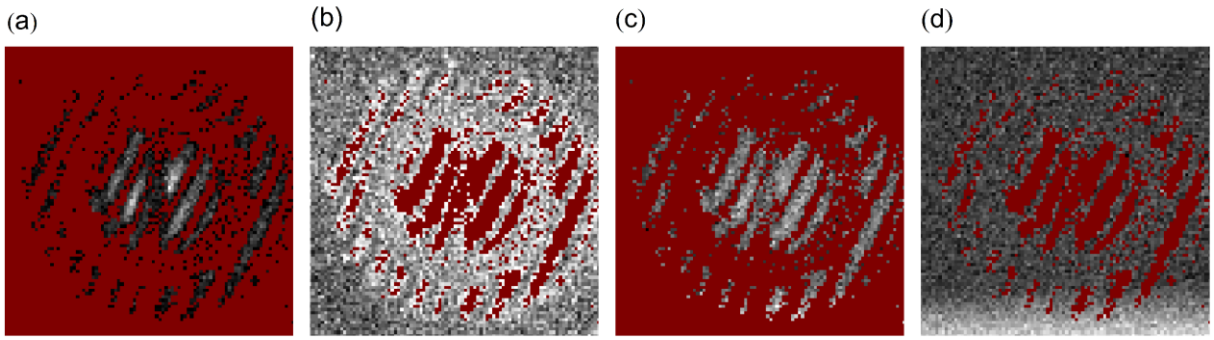

Figure 25. Holograms with masks used for separation between bright and dark region. Hologram recorded with heralded light: (a) shows bright region with mask covering dark region and (b) shows dark region with masks covering bright region. Hologram recorded with non-heralded light: (c) shows bright region with mask covering dark region and (d) shows dark region with masks covering bright region. Red pixels are associated with missing values and grayscale pixels are associated with values used for calculation of signal, noise and SNR for corresponding hologram.

The second object for hologram recordings was a microscope cover glass on a dielectric mirror positioned in the object arm of the interferometer. The cover glass is positioned in a way that it covers approximately one quarter of the field of view. In Figure 26**,** I show holograms of the cover glass and corresponding reconstructions of the amplitude and phase. The hologram obtained with the heralded single photons demonstrates higher contrast than the one obtained with non-heralded light. The amplitude reconstruction shows more distinct borders and surface of the cover glass in the case of recordings with heralded single photons than in the case of non-heralded light. The comparison of the phase image acquired with heralded single photons reveals a larger area with well-defined phase information than the phase images obtained by non-heralded light. On the images with corrected linear phases, the object is clearly distinguished from the surroundings. Outside the area of the detected beam, the phase is random and does not show any interesting feature.

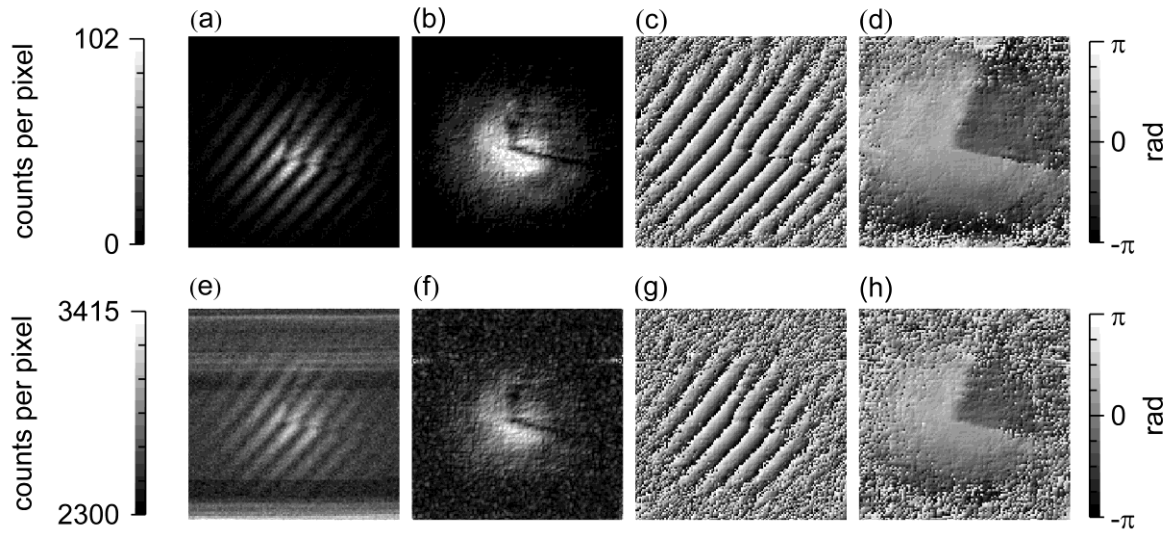

Figure 26. Upper row**:** a hologram recorded with heralded single photons (a); the corresponding amplitude (b); phase reconstruction (c); phase corrected reconstruction (d). Lower row: a hologram recorded with non-heralded light (e); the corresponding amplitude (f); phase reconstruction (g); phase corrected reconstruction (h). Recordings are 136x135 pixel, the integration time is 5 s/pixel and the coincidence time window is 3 ns.

In Figure 26, the visibility near the beam centre of the hologram is 11% for the non-heralded light and 98% for the heralded single photons. The high visibility is possible due to the highly reflective dielectric mirrors positioned in both optical arms of the interferometer. It is also visible from the line profile that the low visibility of non-heralded light is dominated by noise from the imaging detector. The profile from which the visibility was calculated is shown in Figure 27. For the heralded light $N_{max} = 89$ and $N_{min} = 1$ and for the non-heralded light is $N_{max} = 3200$ and $N_{min} = 2570$. The visibility in case of imaging with non-heralded light is better than for the previously recorded object and explains the fact that object is visible at all. Assuming the same detection efficiency and noise, the signal should be increased to 228730 counts / (pixel · 5 s) to achieve the same SNR as for the heralded single-photon states. In other words, for the same minimum, the maximum should be increased 6353 times more than it is used in the case of single-photon states.

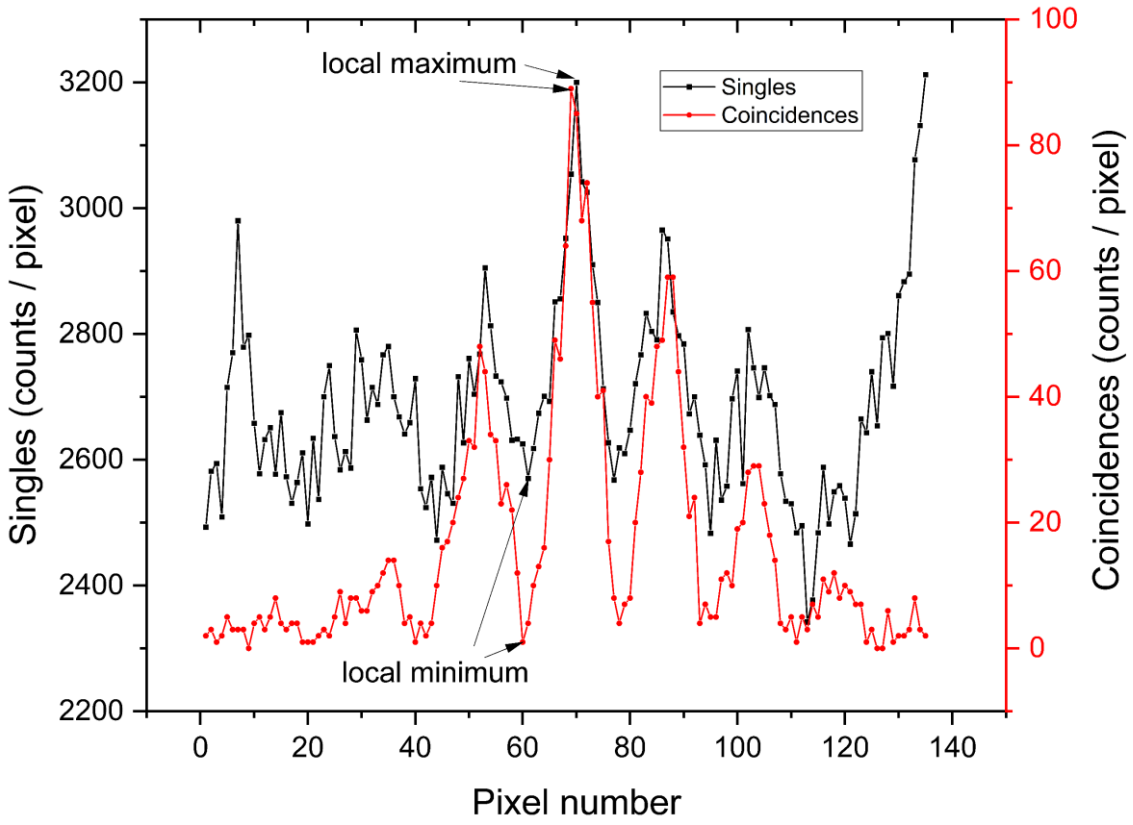

Figure 27. The profile of single line taken from holograms recorded with heralded light (coincidences) and with non-heralded light (singles).

Table V shows quantitative measures for Figure 26. The average count rate on the imaging detector $N_I = 2644(131)$ counts / pixel, the average count rate on the trigger (heralding) detector $N_T = 344564(1782)$ counts / pixel, the average dark count of the imaging detector $N_{DI} = 2476(63)$ counts / (pixel · 5 s), the average dark count of the trigger detector $N_{DT} = 2935(56)$ counts / (pixel · 5 s), and the coincidence time window $\Delta t = 3$ ns according to Equation (43) yields the estimated accidental coincidence noise CN=2.7(1). All predictions (estimated values) agree well with the data (measured values) taken from the hologram acquisition. Table VI also reveals that the estimated detector noise (column: non-heralded light) is the same as in Table III because the same imaging detector was used. The standard deviations are large, but similar to the values obtained for the holograms shown previously. Assuming the same detection efficiency and noise, the signal should be increased to 13200 counts / (pixel · 5 s) to achieve the same SNR as for the heralded single-photon states. In other words, for the same minimum, the maximum should be increased 880 times more than it is used in the case of single-photon states.

Holograms from Figure 26	Single-photon states	Non-heralded light
Measured counts in bright region	18(14)	2644(131)
Measured counts in dark region	3(2)	2640(136)
Estimated noise	2.7(1)	2476(63)
Signal	15(14)	4(189)
SNR measured	6(6)	0.0015(72)
SNR estimated	7(5)	0.002(76)

Table V. Average counts / pixel for the two recorded holograms (Figure 26(a) and (e)) and their SNRs.

The selected bright and dark region are shown in Figure 28. Due to the best overlap between the estimated and measured values, the bright region consists of pixels with count rate >6 and the dark region consists of pixels with count rate ≤6.

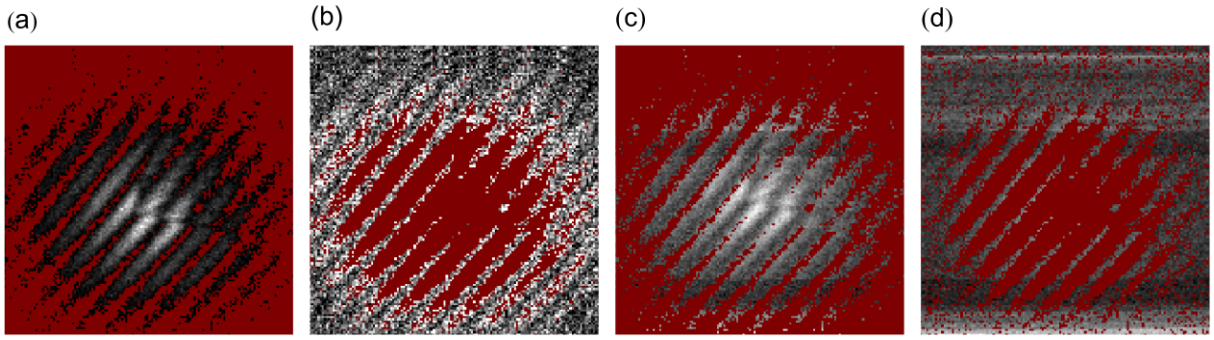

Figure 28. Holograms with masks used for separation between bright and dark region. Hologram recorded with heralded light: (a) shows bright region with mask covering dark region and (b) shows dark region with masks covering bright region. Hologram recorded with non-heralded light: (c) shows bright region with mask covering dark region and (d) shows dark region with masks covering bright region. Red pixels are associated with missing values and grayscale pixels are associated with values used for calculation of signal, noise and SNR for corresponding hologram.

Measurements were also made with cover glass on a dielectric mirror with longer exposure time per pixel and limited field of view. These holograms were recorded with two imaging detectors (SPCM4 and SPCM 5 in Figure 6) behind the interferometer (with imaging lens). Figure 29 shows these holograms recorded with heralded light. The image shown in Figure 29 (c) illustrates that no triple coincidence event was recorded. In this way, the results support the main hypothesis that the holograms were recorded with single-photon states.

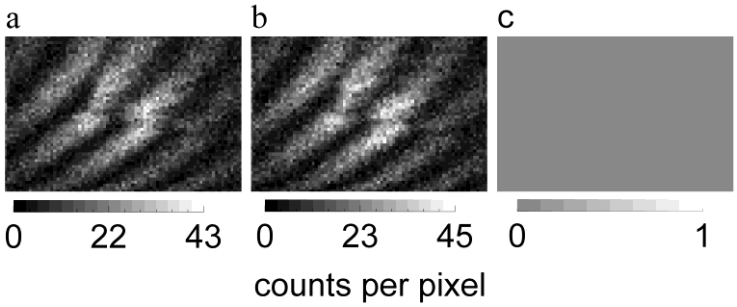

Figure 29. Nonclassical digital holograms recorded with heralded single photons and triple coincidence statistics considering SPCM4 and SPCM5 behind the interferometer. Nonclassical holograms obtained from coincidences between SPCM1 and SPCM4 (a) and coincidences between SPCM1 and SPCM5 (b) are shown. Finally, triple coincidences between SPCM1, SPCM4 and SPCM5 are shown in (c). The hologram is 77x51 pixels, the integration time is 10 s/pixel and the coincidence time window is 3 ns.

To compare the fringe signal-to-noise ratio of the hologram recordings for heralded and non-heralded light, line holograms were taken with a larger integration time per pixel. A horizontal line, consisting of *m* pixels, was chosen from Figure 26, where the pattern is not disturbed by the object. The line was scanned with an exposure time of 20 s per pixel. The long exposure time facilitated the data results so that a curve fit could be made even for previously blurred fringes obtained with non-heralded light.

In Figure 30, the one-dimensional fringe of the holograms, ydata, and fitting curve, y, for heralded (a) and non-heralded b) light is presented. The fitting function is taken as:

$$y(x) = Y_0 + A\exp\left[-\frac{(x-x_0)^2}{2w^2}\right][1 + B\sin(\omega x + \varphi)] \tag{49}$$

represents sinusoidal fringes convoluted with a Gaussian function coming from the beam profile. The noise of the signal was calculated as the root mean squared of residuals: $N = \sqrt{\sum_{i=1}^{m}(y_i - ydata_i)/m}$, and for the signal, the difference between the maximum and minimum of the data was taken, $S = \max(y) - \min(y)$. The fringe signal-to-noise ratio, SNR_f = S/N, for heralded and non/heralded recordings is SNR_{fh} = 18.8 and SNR_{fnh} = 2.6, respectively.

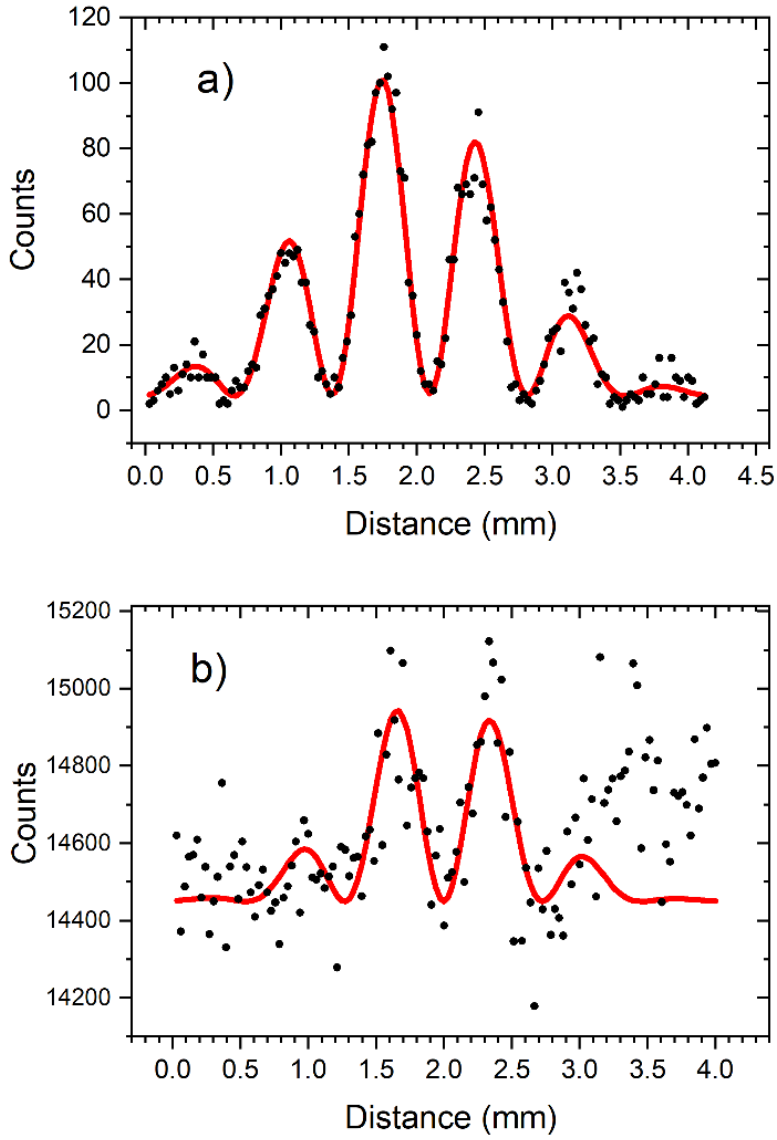

Figure 30. Line holograms are recorded with heralded light (a) and non-heralded light (b). The integration time is 20 s/pixel, experimental data (scatter) and fit (line).

5 Discussion

5.1 Single-photon experiments and single-photon interference

Generally, single-particle experiment and single-particle interference is manifested as absences of two and more photons. In order to measure the absence of two and more photons it is necessary to have suitable single-particle source and particle number resolving detection system. If one detector without particle number resolving characteristics is used, then it is not possible to characterize the state generated by the source. If two detectors without particle number resolving characteristics are used, then it is possible to imitate particle number resolving detection system. After collecting sufficient particle statistics then is possible to conclude what kind of source was used.

The interference pattern predicted by classical wave theory seemingly resembles the prediction of quantum theory with single particles. However, the difference is fundamental, the quantum theory of single particles predicts single localizable events for which only probability can be given due to indeterministic feature of quantum physics, and classical wave theory predicts continuous fringe pattern based on deterministic feature of classical physics. In case of strongly attenuated classical wave, the amplitude is reduced, but the continuous fringe pattern is still expected to be visible. When the classical light source is strongly attenuated, it is still possible to have two and more detection events simultaneously. Usage of highly attenuated classical light source or highly inefficient detection system or single pixel detection system can only mimic the single-photon detection but cannot reproduce the photon statistics expected from single-photon source. One could argue that at the single photon level, it is not possible to see the interference fringes, but only when sufficient photon statistics is accumulated, the interference fringes appear. Anyway, in its fundamental nature, these fringes are from the very beginning different from fringes predicted by the classical wave theory, because in single-photon experiment they are localizable as single grainy points at the detection plane. Specifically, the detection of two and more detection events is in sharp contrast to single-photon experiment.

It is an open question how a single-photon states can imitate a classical interference pattern that contains whole information about a three-dimensional physical object. Quantumly speaking, individual photons (with his unknown location in the Gaussian beam profile) randomly illuminate an object, and it is not obvious how they can collectively transmit amplitude and phase information about the object. In other words, instead of clear deterministic mechanism,

only accumulation of single random events appears. Detected single random events then gradually (and seemingly) resemble the classically predicted interference fringes. From classical physics, this solution to this issue is clear, because the physics is deterministic, well described by mathematics of continuum, and no granularity is expected. However, the experiments show that this picture breaks apart not only because of the nature of photodetection, but because of the single photon nature of the single photon source. The single photon behaviour of the single photon source is not reproducible from classical physics in terms of photon statistics. It is always necessary to have in mind that the interference pattern in the case of the true single-particle experiment is a construct of the accumulated true single-particle detections generated by the true single-particle source, and is therefore very different from classical physics, where one would expect more than single detection events in the interference pattern simultaneously.[1] A quantitative criterion that could distinguish between the true single particle experiment and classical experiment can be given by using the second order correlation function (as previously defined). Interestingly, the most or even all previous interference experiments with single photons did not provide measurement of the second order correlation function during acquisition of interference pattern. In here presented experiment, I provide a way to measure the fundamental nature of light source during interference acquisition. It is also interesting to note that is often assumed that pixel-by-pixel imaging provides only incoherent image information [77], but here the heralded single-photon experiment shows that imaging with single-pixel scanning preserves amplitude and phase information at the same time.

5.2 Phase of single photon

Classical holography relies on the reference and object wave for hologram recordings. In the case of a single particle in a holographic setup, the role of the classical reference and classical object wave is obscured due to the indivisible character of the single particle. This contrasts with classical waves, which can be divided into reference and object waves as well as detected simultaneously at several places at once. Conceptually, the biggest difference between quantum and classical holographic approaches is in the fact that the classical approach does not include the single-particle nature of quantum phenomena and their probabilistic character. The retrieval

[1] The same is true for single particle experiments without interference pattern.

of the phase from a hologram with single photons is considered a challenging task due to the indeterminate global phase of single photons [61, 63, 78] and can be potentially obscured by the nature of the recording.
The quantum probability amplitude can be written simplified as

$$\psi(\vec{r},t) = f(\vec{r})\exp\left(i\theta(t)\right) \tag{50}$$

where $\vec{r}$ is the position vector of the particle in three dimensions at some time t and θ is the global phase factor θ. As interpreted by Born's probability rule, the square of the modulus of the wave function gives the probability of the position in which the photon can be found. However, the global phase factor θ is arbitrarily defined and thus does not provide information about the local phase of a single photon.

It may appear puzzling to record a hologram with number states because for single-particle states or for any precisely defined Fock states, the quantum phase cannot be measured simultaneously with an arbitrarily high precision [79]. Theoretically, the interference effects can be obtained due to the phase-dependent normal-mode expansion of the quantized electromagnetic field and its corresponding time evolution [80]. However, no conclusive experimental evidence of a successful hologram recording with single-photon states has been demonstrated until now.

The results of our experiment with single-photon source and the implemented continuous monitoring of the light source in front of the interferometer strongly indicate the non-classical nature of the illumination and the non-classical origin of the holograms recorded with single-photon states. A more ideal experiment with larger number of single-photon states and better (with higher efficiency and lower dark count rates) photon-number-resolving detectors behind the interferometer would be necessary for fully conclusive evidence, for example against the argument that the light behaves differently in the characterization setup before the interferometer than behind the interferometer.

5.3. Evidence for quantum interpretation of the basic principle of holography

Typically, textbook descriptions [46] show these basic equations of holography in terms of wave functions but do not point out the fundamental difference between classical and quantum descriptions of the complex wave function. Complex wave functions do not have the same physical meaning in quantum physics and electromagnetic theory. Quantum theory deals with probability amplitude, while Maxwell's electromagnetic theory is a deterministic theory. Quantum theory seems to require a description based on complex numbers [81, 82], and electromagnetic theory uses complex numbers just as a convenient calculational tool. Therefore, I cautiously distinguish between quantum and classical holography equations due to their different meanings in relation to the physical world. As shown in section 2.6, the coding process can be described as the quantum superposition of a single particle. Of course, as Gabor [1] invented, the success of the coding process is shown by a successful decoding process of the phase and amplitude information. From a fundamental point of view, the quest for the photon wave function can be seen as a deep and still open problem [83], so in this context, the basic holography equations for a single photon have yet to be found. In this work, I follow the experimental approach to holography from the quantum, single-particle perspective. The single-particle perspective is supported by the measurement of photon statistics, in particular the second order correlation function $g^{(2)}(0)$.

A system based on a single-photon state is the simplest system in which the difference between classical and quantum descriptions of the basic holographic equations is visible. The classical description of the basic holographic equations relies on having two beams of light, the reference beam and the object beam. There exists no conceptual challenge to generate the reference beam and the object beam by splitting the classical amplitude into two parts with a beam splitter. However, quantum description at the level of a single photon does not permit real physical entities at two places at the same time. An ingenious solution based on one-photon probability for imaging objects in front of an interferometer has been found [63]. Although the elegant method for imaging objects outside an interferometer and the beauty of this experiment due to the use of a two-dimensional detector are evident, the photon statistics in terms of single-photon illumination (second order correlation function and the violation of the classical bound) are challenging to obtain during two-dimensional hologram acquisition. In contrast to this method, I showed quantitative data about the photon illumination statistics to support the description of hologram recording from a single photon view. Another advantage of here presented method is that it is possible to record a hologram without prior knowledge about object-specific spatial

frequencies. It is also important to mention that the (modified) Michelson interferometer is easily tuneable for various off-axis configurations, and with the numerical method used, only one hologram image is enough for the extraction of both amplitude and phase information.

The implemented continuous monitoring of the light source assures the nonclassical illumination and nonclassical origin of the holograms. Due to the monitoring part of the setup, the proposed setup for recording nonclassical holograms with single photons could distinguish between classical light sources or quantum light during the experimental measurement. If someone would insist that the holograms are not non-classical in nature, then one would need to construct a light source and setup for recording holograms not just in low-light-level regime (based on detectors sensitive to single photons), but one would need to reach at least $g^{(2)}(0) \geq 1$ at the same time. Since our light source and detection protocol shows that I record holograms with single photons which have $g^{(2)}(0) << 1$, one is thus led to conclude that the here implemented protocol with single-photon states is purely quantum in nature.

5.4. Image contrast enhancement with heralded single photon source

In contrast to previous experiments in dim light, I have also shown that it is possible to record quantum holograms with single-photon states that surpass classical holograms recorded with non-heralded light in terms of image contrast under similar intensity. SNR and visibility of holograms as defined (see section 4.3.) appears to be a good measure of object visibility under the given circumstances. A stronger light source is an attractive alternative to make to the object visible, but this is not always a viable option. Strong illumination cannot be hidden, and it could change the properties of the object or even damage the object. In these scenarios, the heralded method can be particularly useful because it can enable covert imaging and low-light-level imaging. Another suitable scenario for usage of heralded method is in case of strong intrinsic noise of the light generation and detection system, or external noise introduced for example by stray light and turbulences during light propagation.

6 Conclusion and outlook

In contrast to previous work, the presented experiment demonstrates a difference between classical and quantum holography in a system based on single-photon states and a basic holographic interferometer. Continuous measurement of photon statistics during (nonclassical) hologram recording excludes the possibility of a description based on classical wave theory. Compared to classical illumination, the measurements with single-photon states and slightly less intensity show strong improvement of contrast on both amplitude and phase reconstruction. This advantage can be useful for recording holograms in low-light-level conditions, in the presence of background noise, and for avoiding the use of expensive detectors with low dark count rates. A question of whether further improvement of the signal-to-noise ratio is achievable, with different settings, will remain open for further research.

There are many more interesting questions that could be researched in follow-up projects. Here, I give my personal list of possible future research topics in quantum holography (imaging):

1) application of single-photon states in quantum holography without coincidence technique
2) application of two-photon (or more generally N-photon) states for quantum holography with increased phase sensitivity
3) application of polarization entangled photon pairs for recording polarization sensitive objects
4) investigation of the differences between pulsed laser (coherent states) and single-photon states
5) recording of holograms with a minimum number of photons and increased spatial resolution
6) investigation of limits in accuracy and precision in determination of the phase with and without coincidence techniques
7) investigation of quantum hologram recordings with different types of photosensors
8) quantum holography without a lens (Fresnel holography)

In all these questions, the phase of a single photon has or could play an important role, and it would be an interesting opportunity to provide a complementary theoretical framework for the phase of the single-photon states dependent on the realized experimental configuration.

7 References

1. Gabor, D., New Microscopic Principle, *Nature* **161** 777–778 (1948).
2. Aharonov, Y. & Bohm, D., Significance of Electromagnetic Potentials in the Quantum Theory, *Phys. Rev.* **115**, 485–491 (1959).
3. Tonomura, A., Osakabe, N., Matsuda, T., Kawasaki, T., Endo, J., Yano, S. & Yamada, H., Evidence for Aharonov-Bohm effect with magnetic field completely shielded from electron wave, *Phys. Rev. Lett.* **56**, 792–795 (1986).
4. Planck, M., Über das Gesetz der Energieverteilung im Normalspektrum, *Ann. Phys.* **309**, 553–563 (1901).
5. Einstein, A., Über einen die Erzeugung und Verwandlung des Lichtes betreffenden heuristischen Gesichtspunkt, *Ann. Phys.* **322**, 132–148 (1905).
6. Klein, M. J., Thermodynamics and quanta in Planck's work, *Phys. Today* **19**, 23–32 (1966).
7. Millikan, R. A., A Direct Photoelectric Determination of Planck's " h ". *Phys. Rev.* **7**, 355–388 (1916).
8. Compton, A. H., The Spectrum of Scattered X-Rays, *Phys. Rev.* **22**, 409–413 (1923).
9. Einstein, A., Zur Quantentheorie der Strahlung, *Phys. Z.* **18**, 121 (1917).
10. Klemperer, O., On the annihilation radiation of the positron, *Math. Proc. Camb. Phil. Soc.* **30**, 347–354 (1934).
11. Dunker, T., Who discovered positron annihilation? Preprint at http://arxiv.org/abs/1809.04815 (2022).
12. Thorn, J. J., Neel, M. S., Donato, V. W., Bergreen, G. S, Davies, R. E. & Beck, M., Observing the Quantum Behavior of Light in an Undergraduate Laboratory, *Am. J. Phys.* **72**, 1210 (2004).
13. Clauser, J. F., Experimental distinction between the quantum and classical field-theoretic predictions for the photoelectric effect, *Phys. Rev. D* **9**, 853–860 (1974).
14. Young, T., The Bakerian Lecture. Experiments and calculations relative to physical optics, *Phil. Trans. R. Soc.* **94**, 1–16 (1804).
15. Taylor, G.I., Interference fringes with feeble light, *Prec. Cambridge Philos. Soc.* **15**, 114 (1909).
16. Zeilinger, A., Gähler, R., Shull, C. G., Treimer, W. & Mampe, W., Single- and double-slit diffraction of neutrons, *Rev. Mod. Phys.* **60**, 1067–1073 (1988).

17. Tonomura, A., Endo, J., Matsuda, T., Kawasaki, T. & Ezawa, H., Demonstration of single-electron buildup of an interference pattern, *Am. J. Phys.* **57**, 117–120 (1989).
18. Arndt, M., Nairz, O., Vos-Andreae, J., Keller, C., Van Der Zouw, G., & Zeilinger, A., Wave–particle duality of C60 molecules, *Nature* **401**, 680–682 (1999).
19. Jacques, V., Wu, E., Toury, T., Treussart, F., Aspect, A., Grangier, P. & Roch, J.-F., Single-photon wavefront-splitting interference: An illustration of the light quantum in action. *Eur. Phys. J. D* **35**, 561–565 (2005).
20. Feynman, R. P., Leighton, R. B., Sands, M., *The Feynman Lectures on Physics*. (Addison-Wesley, Reading, Massachusetts, 1966., Vol. 3 Ch. 1)
21. Catani, L., Leifer, M., Schmid, D. & Spekkens, R. W., Why interference phenomena do not capture the essence of quantum theory. Preprint at http://arxiv.org/abs/2111.13727 (2022).
22. Feynman, R. P., Leighton, R. B., Sands, M., *The Feynman Lectures on Physics* (Addison-Wesley, Reading, Massachusetts, 1966., Vol. 3 Ch. 3)
23. Einstein, A., Podolsky, B. & Rosen, N., Can Quantum-Mechanical Description of Physical Reality Be Considered Complete?, *Phys. Rev.* **47**, 777–780 (1935).
24. Bohm, D. *Quantum Theory* (Prentice-Hall, Englewood Cliffs, NJ, 1951).
25. Bohm, D. & Aharonov, Y., Discussion of Experimental Proof for the Paradox of Einstein, Rosen, and Podolsky, *Phys. Rev.* **108**, 1070–1076 (1957).
26. Bohm, D., A, Suggested Interpretation of the Quantum Theory in Terms of 'Hidden' Variables. I., *Phys. Rev.* **85**, 166–179 (1952).
27. Bell, J.S., On the Einstein Podolsky Rosen Paradox, *Physics* **1**, 195 (1964).
28. Clauser, J. F., Horne, M. A., Shimony, A. & Holt, R. A., Proposed Experiment to Test Local Hidden-Variable Theories, *Phys. Rev. Lett.* **23**, 880–884 (1969).
29. Freedman, S. J. & Clauser, J. F. Experimental Test of Local Hidden-Variable Theories, *Phys. Rev. Lett.* **28**, 938–941 (1972).
30. Aspect, A., Grangier, P. & Roger, G., Experimental Tests of Realistic Local Theories via Bell's Theorem. *Phys. Rev. Lett.* **47**, 460–463 (1981).
31. Aspect, A., Grangier, P. & Roger, G., Experimental Realization of Einstein-Podolsky-Rosen-Bohm Gedankenexperiment: A New Violation of Bell's Inequalities, *Phys. Rev. Lett.* **49**, 91–94 (1982).
32. Aspect, A., Dalibard, J. & Roger, G., Experimental Test of Bell's Inequalities Using Time- Varying Analyzers, *Phys. Rev. Lett.* **49**, 1804–1807 (1982).

33. Giustina, M. *et al.*, Significant-Loophole-Free Test of Bell's Theorem with Entangled Photons, *Phys. Rev. Lett.* **115**, 250401 (2015).
34. Hensen, B. *et al.*, Loophole-free Bell inequality violation using electron spins separated by 1.3 kilometres, *Nature* **526**, 682–686 (2015).
35. Shalm, L. K. *et al.*, Strong Loophole-Free Test of Local Realism. *Phys. Rev. Lett.* **115**, 250402 (2015).
36. Clauser, J. F. & Shimony, A. Bell's theorem. Experimental tests and implications, *Rep. Prog. Phys.* **41**, 1881–1927 (1978).
37. Horodecki, R., Horodecki, P., Horodecki, M. & Horodecki, K., Quantum entanglement, *Rev. Mod. Phys.* **81**, 865–942 (2009).
38. Gerry, C. & Knight, P., Introductory Quantum Optics. (Cambridge University Press, 2004).
39. Boyd R. W., *Nonlinear optics*. (Academic press, New York, 2008).
40. Couteau, C., Spontaneous parametric down-conversion, *Contemp. Phys.* **59**, 291–304 (2018).
41. Burnham, D. C. & Weinberg, D. L., Observation of Simultaneity in Parametric Production of Optical Photon Pairs. *Phys. Rev. Lett.* **25**, 84–87 (1970).
42. Joobeur, A., Saleh, B. E. A. & Teich, M. C., Spatiotemporal coherence properties of entangled light beams generated by parametric down-conversion, *Phys. Rev. A* **50**, 3349–3361 (1994).
43. Fedrizzi, A., *Fundamental experiments with a high brightness source of entangled photons*. (PhD thesis, University of Vienna, 2008).
44. Cova, S., Ghioni, M., Itzler, M.A., Bienfang, J.C., Restelli, A., *Semiconductor-Based Detectors*, in. Migdall, A., Polyakov, S., Fan, J. & Bienfang, J. (eds), *Single-Photon Generation and Detection: Physics and Applications* (Academic Press, 2013)
45. Photonics Media. 2022/02/18 Webinar: Single-Photon Detectors and Detection: SiPM, SPAD, SNSPD, PMT, TES.
46. Collier, R. Burckhardt, C. B., Lin, L. H., *Optical holography*. (Academic Press, New York 2013).
47. Mertz, J., *Introduction to Optical Microscopy*, 2nd ed. (Cambridge University Press, 2019).
48. Kim, M. K., *Digital Holographic Microscopy: Principles, Techniques, and Applications* (Springer New York, New York, NY, 2011).

49. Kim, M. K., Principles and Techniques of Digital Holographic Microscopy, *J. Photonics. Energy*, 018005 (2010).
50. Demoli, N., Lectures in Optics and Holography, Doctoral study in physics, University of Zagreb, Faculty of Science, Zagreb 2017.
51. Mandel, L. & Wolf, E., Optical Coherence and Quantum Optics. (Cambridge University Press 1995).
52. Blauensteiner, B., Herbauts, I., Bettelli, S., Poppe, A. & Hübel, H., Photon Bunching in Parametric Down-Conversion with Continuous-Wave Excitation, *Phys. Rev. A* **79**, 063846 (2009).
53. Lloyd, S., Enhanced sensitivity of photodetection via quantum illumination, *Science* **321**, 1463 (2008).
54. Lopaeva, E. D., Ruo Berchera, I., Degiovanni, I. P., Olivares, S., Brida, G. & Genovese, M., Experimental Realization of Quantum Illumination, *Phys. Rev. Lett.* **110**, 153603 (2013).
55. Boto, A. N., Kok, P., Abrams, D. S., Braunstein, S. L., Williams, C. P., and Dowling, J. P., Quantum interferometric optical lithography: exploiting entanglement to beat the diffraction limit, *Phys. Rev. Lett.* **85**, 2733 (2000).
56. D'Angelo, M., Chekhova, M. V. and Shih, Y., Two-photon diffraction and quantum lithography, *Phys. Rev. Lett.* **87**, 013602 (2001).
57. England, D. G., Balaji, B. and Sussman, B. J., Quantum-enhanced standoff detection using correlated photon pairs, *Phys. Rev. A* **99**, 023828 (2019).
58. Hirano, I. & Hirai, N. Holography in the single-photon region, *Appl. Opt.* **25**, 1741 (1986).
59. Yamamoto, M., Yamamoto, H. & Hayasaki, Y., Photon-counting digital holography under ultraweak illumination, *Opt. Lett.* **34**, 1081 (2009).
60. Demoli, N., Skenderović, H. & Stipčević, M., Digital holography at light levels below noise using a photon-counting approach, *Opt. Lett.* **39**, 5010 (2014).
61. Chrapkiewicz, R., Jachura, M., Banaszek, K. & Wasilewski, W., Hologram of a single photon, *Nature Photon* **10**, 576–579 (2016).
62. Defienne, H., Ndagano, B., Lyons, A. & Faccio, D., Polarization entanglement-enabled quantum holography, *Nat. Phys.* **17**, 591–597 (2021).
63. Szadowiak, W., Kundu, S., Szuniewicz, J. & Lapkiewicz, R., Self-referenced hologram of a single photon beam, *Quantum* **5**, 516 (2021).

64. Töpfer, S., Gilaberte Basset, M., Fuenzalida, J., Steinlechner, F., Torres, J. P. & Gräfe M., Quantum holography with undetected light, *Sci. Adv.* **8**, eabl4301 (2022).
65. Ma, X., Zotter, S., Kofler, J., Jennewein, T. & Zeilinger, A. Experimental generation of single photons via active multiplexing, *Phys. Rev. A* **83**, 043814 (2011).
66. Jin, R.-B., Fujiwara, M., Yamashita, T., Miki, S., Terai, H., Wang, Z., Wakui, K., Shimizu, R., & Sasaki M., Efficient detection of an ultra-bright single-photon source using superconducting nanowire single-photon detectors, *Opt. Comm.* **336**, 47–54 (2015).
67. Grangier, P., Roger, G. & Aspect, A., Experimental Evidence for a Photon Anticorrelation Effect on a Beam Splitter: A New Light on Single-Photon Interferences, *Europhys. Lett.* **1**, 173–179 (1986)
68. Yang, J.-Z., Li, M.-F., Chen, X.-X., Yu, W.-K., and Zhang, A.-N. Heralded single-pixel imaging with high loss-resistance and noise-robustness, *Appl. Phys. Lett.* **117**, 214001 (2020).
69. Kwiat, P. G. & Chiao, R. Y., Observation of a nonclassical Berry's phase for the photon, *Phys. Rev. Lett.* **66**, 588–591 (1991).
70. Devaux, F., Mosset, A., Bassignot, F. & Lantz, E., Quantum holography with biphotons of high Schmidt number, *Phys. Rev. A* **99**, 033854 (2019).
71. Grünwald, P., Effective second-order correlation function and single-photon detection, *New J. Phys.* **21**, 093003 (2019).
72. Personal communication with Integrated Optics (manufacturer)
73. Kuklewicz, C.E., *Ultrabright source of polarization-entangled photons from cavity-enhanced downconversion*. (PhD thesis, MIT, 2006)
74. Stipčević, M., Skenderović, H. & Gracin, D., Characterization of a novel avalanche photodiode for single photon detection in VIS-NIR range, *Opt. Express* **18**, 17448 (2010).
75. Excelitas SPCM-AQRH Family datasheet, https://www.excelitas.com/file-download/download/public/60241?filename=Excelitas_SPCM-AQRH_Family_datasheet.pdf
76. Eisaman, M. D., Fan, J., Migdall, A. & Polyakov, S. V., Invited Review Article: Single-photon sources and detectors, *Rev. Sci. Instrum.* **82**, 071101 (2011).
77. Bennink, R. S., Bentley, S. J., Boyd, R. W. & Howell, J. C., Quantum and Classical Coincidence Imaging, *Phys. Rev. Lett.* **92**, 033601 (2004).

78. Lvovsky, A. I., Hansen, H., Aichele, T., Benson, O., Mlynek, J. & Schiller, S., Quantum State Reconstruction of the Single-Photon Fock State, *Phys. Rev. Lett.* **87**, 050402 (2001).
79. Heitler, W., *Quantum Theory of Radiation* (Oxford, London, 1954).
80. Langangen, Ø., Vaskinn, A. & Skagerstam, B.-S., Interference of Light in a Michelson-Morley Interferometer: A Quantum Optical Approach, International Journal of Optics **2012**, 1–10 (2012).
81. Li, Z.-D. et al., Testing Real Quantum Theory in an Optical Quantum Network, *Phys. Rev. Lett.* **128**, 040402 (2022).
82. Chen, M.-C. et al. Ruling Out Real-Valued Standard Formalism of Quantum Theory, *Phys. Rev. Lett.* 128, 040403 (2022).
83. Kiessling M. K.-H. & Tahvildar-Zadeh A. S., On the quantum-mechanics of a single photon, *J. Math. Phys.* **59**, 112302 (2018).

8 Author biography

Denis Abramović completed his taught master's degree in physics at the University of Zagreb, Faculty of Science, Department of Physics and later master's degree in physics (MSc) at the University of Vienna in 2015. He did his MSc thesis in the group of Anton Zeilinger at the Institute of Quantum Optics and Quantum Information - Vienna. Since 2016, he started working as a research assistant in the group of Nazif Demoli and later in the group of Hrvoje Skenderović, both at the Institute of Physics in Zagreb. He is co-author of four published (plus one submitted) scientific articles in CC journals, one popular article and five conference presentations about the dissertation topic, including one invited talk.

List of publications:

1. A. M. Dezfouli, D. Abramović, M. Rakić, and H. Skenderović, Simultaneous Generation and Detection of Multiple Orbital Angular Momentum States Using a Single Phase-Only Optical Element, (submitted 2023).

2. D. Abramović, N. Demoli, M. Stipčević, and H. Skenderović, Quantum Holography with Single-Photon States, (2022). https://doi.org/10.48550/arXiv.2209.00431 (submitted 2022, accepted Phys. Rev. A 2023).

3. A. M. Dezfouli, D. Abramović, M. Rakić, and H. Skenderović, Detection of the Orbital Angular Momentum State of Light Using Sinusoidally Shaped Phase Grating, *Appl. Phys. Lett.* **120**, 191106 (2022).

4. N. Demoli, D. Abramović, O. Milat, M. Stipčević, and H. Skenderović, Linearity and Optimum-Sampling in Photon-Counting Digital Holographic Microscopy, *Photonics* **9**, 68 (2022).

5. N. Demoli, J. Gladić, D. Lovrić, and D. Abramović, Digital Holography Using LCOS Microdisplay as Input Three-Dimensional Object, *Optik* 194, 162877 (2019).

Selected conference presentations:

1. D. Abramović, N. Demoli, M. Stipčević, and H. Skenderović, Quantum Holography with Heralded Single-photon Source, *Conference on Lasers and Electro-Optics Europe / European Quantum Electronics Conference* (CLEO/Europe-EQEC), session EA-6.2, 26 - 30 June 2023, Munich, Germany (oral presentation).

2. D. Abramović, H. Skenderović, Heralded Single Photons for Holography, *Sensing with Quantum Light*, 790. WE-Heraeus-Seminar, 4-7 June 2023 Bad Honnef, Germany (poster presentation).

3. D. Abramović, N. Demoli, H. Skenderović, Heralded Single Photons for Holography, *Imaging and Applied Optics Congress* 2022 (3D, AOA, COSI, ISA, pcAOP), Technical Digest Series (Optica Publishing Group, 2022), paper CM1A.7., 11–15 July 2022, Vancouver, British Columbia Canada (on-line oral presentation).

4.. D. Abramović, N. Demoli, H. Skenderović, Application of Single Photons in Holography, *EGAS 52nd*, July 6-8, 2021, Zagreb, Croatia (on-line poster presentation).

5. D. Abramović, N. Demoli, H. Skenderović, Single-photon Holography, *14th Photonics Workshop*, 14-17 March 2021, , Kopaonik, Serbia (invited on-line oral presentation).